

Evolution of Spatial Complexity in Flare Ribbon Substructure and Its Relationship to Magnetic Reconnection Dynamics

MARCEL F. CORCHADO ALBELO,^{1,2,3,*} MARIA D. KAZACHENKO,^{1,2,3} RYAN J. FRENCH,³ VADIM M. URITSKY,^{4,5}
EMILY MASON,⁶ COLE A. TAMBURRI,^{1,2,3,*} RAHUL YADAV,³ AND BENJAMIN J. LYNCH^{7,8}

¹*Department of Astrophysical and Planetary Sciences, University of Colorado Boulder, 2000 Colorado Avenue, Boulder, CO 80305, USA*

²*National Solar Observatory, 3665 Discovery Drive, Boulder, CO 80303, USA*

³*Laboratory for Atmospheric and Space Physics, University of Colorado Boulder, 3665 Discovery Drive, Boulder, CO 80303, USA*

⁴*Catholic University of America 620 Michigan Ave., N.E. Washington, DC, 20064, USA*

⁵*NASA Goddard Space Flight Center 8800 Greenbelt Ave. Greenbelt, MD, 20771, USA*

⁶*Predictive Science Inc., 9990 Mesa Rim Rd., Suite 170, San Diego, CA 92121, USA*

⁷*Space Sciences Laboratory, University of California, Berkeley, CA 94720, USA*

⁸*Department of Earth, Planetary, and Space Sciences, University of California, Los Angeles, CA 90095, USA*

ABSTRACT

Recent three-dimensional flare models suggest that flare-ribbon substructure is linked to the fragmentation of the reconnecting current sheet in the corona. Flare-ribbon substructure can therefore potentially serve as a unique diagnostic tool for physical processes in the flare current sheet. In this paper, we describe a new method to quantify the evolution of ribbon substructure, which first extracts the ribbon's leading bright front and then quantifies its morphology using the box-counting dimension and Correlation Dimension Mapping (CDM). We first test our method using synthetic observations. We then apply it to an M6.5-class solar flare on 2015 June 22 observed by the Interface Region Imaging Spectrograph (IRIS) 1330 Å Slit-Jaw Imager (SJI). We find that when the flare ribbon boundary has more multi-spatial-scale features (higher box-counting dimension), hard X-ray (HXR) emission and magnetic-reconnection rates are the strongest. We also find that the flare-ribbon complexity characterized by CDM has moderate correlation with the IRIS Si IV 1402.77 Å non-thermal velocity (in the negative-polarity ribbon) and reconnection flux rates (in ribbons of both magnetic polarities). We conclude that the build-up of the spatial complexity of the ribbons at multiple spatial scales can serve as an observational proxy for current-sheet fragmentation in the corona.

Keywords: Magnetic Reconnection, Solar Flares, Plasma Instabilities, Current Sheets

1. INTRODUCTION

Solar flares are characterized by localized emission of light within the solar atmosphere, spanning the full electromagnetic spectrum from radio waves to γ -rays (see the review by Benz 2017). They are understood to be associated with the release of free magnetic energy stored in twisted and sheared coronal magnetic fields via magnetic reconnection (see reviews by Priest & Forbes 2002; Hudson 2011; Shibata & Magara 2011). In two dimensions (2D), the relationship between magnetic energy release and the transport of mass, heat, and non-thermal particles during the flare can be described by the CSHKP or the standard two-ribbon flare model (Carmichael 1964; Sturrock 1966; Hirasawa 1974; Kopp & Pneuman 1976). An extension to three dimensions (3D) includes a similar physical description and is better suited to explain flare observations (Longcope et al. 2007; Aulanier et al. 2012, 2013; Janvier et al. 2013). Particles accelerated during the flare through bremsstrahlung can produce hard X-rays and γ -rays (Brown 1971). In addition, heated plasma fronts traveling along the magnetic field lines can heat the chromosphere and enhance the emission at various wavelengths (e.g. H α and ultraviolet; Magara et al. 1996; Huang et al. 2014). The localized areas of enhanced emission (e.g. 1330 Å, 1400 Å, 1600 Å, and 1700 Å) in the upper chromosphere (\approx 1000 to 2000 km above the solar sur-

face) are called flare ribbons (e.g. Forbes 2000; Fletcher & Hudson 2001; Qiu et al. 2012; Kazachenko et al. 2017). The brightest and most compact sources of flare-ribbon emission are referred to as flare kernels (Donnelly 1971; Kurokawa et al. 1988; Kitahara & Kurokawa 1990; Warren & Warshall 2001; Alexander & Coyner 2006; Nishizuka et al. 2009; Kowalski et al. 2017). The morphology of flare ribbons is interpreted as a signature of heat and non-thermal particles precipitating from a coronal reconnecting source into the dense chromosphere at the footpoints of newly reconnected flare loops (Forbes & Priest 1984; Forbes 2000; Fletcher & Hudson 2001; Asai et al. 2004; Qiu et al. 2012; Longcope 2014; Graham & Cauzzi 2015; Li et al. 2017; Priest & Longcope 2017; Afanasyev et al. 2023; Fan et al. 2024).

Some observational studies have focused on exploring the emission morphology of the so-called flare ribbon fine-structure or substructure to better understand the mechanisms through which energy is released and transported in the corona and chromosphere during a flare (Bárta et al. 2011; Karlický 2014; Jing et al. 2016; Parker & Longcope 2017; French et al. 2021; Kazachenko et al. 2022; Pietrow et al. 2024; Thoen Faber et al. 2025; Yadav et al. 2025; French et al. 2025b). In particular, observations of wave and swirl-like structures (Brannon et al. 2015; Li & Zhang 2015; Parker & Longcope 2017), ribbon front fragmentation (Naus et al. 2022; Cannon et al. 2023; Polito et al. 2023), quasi-periodic pulsations (Clarke et al. 2021) and bursty flare emission (Collier et al. 2024; Purkhart et al. 2025; French et al. 2025a) demonstrate that flare ribbons are spatial-temporal fragmented structures. Corchado Albelo et al. (2024) showed that the magnetic reconnection rates derived from flare ribbon observations are related to particle acceleration for dozens of flares of various classes. Furthermore, for two of the flares in their study flare ribbon spatial-substructure is observed co-temporally with enhancements in the reconnection flux rates.

The plasmoid (or tearing-mode) instability (Furth et al. 1963; Loureiro et al. 2007; Uzdensky et al. 2010; Huang & Bhattacharjee 2012; Comisso et al. 2017) has been invoked as a theoretical explanation of the spatial-temporal fragmentation of flare ribbon emission in connection to magnetic reconnection dynamics, and has been applied to numerical experiments of solar eruptions (Karpen et al. 2012; Lynch et al. 2016). In flares, the plasmoid instability arises when the flaring current sheet becomes unstable and tears, and subsequently forms plasmoids, flux ropes, or magnetic islands in 2D, within the current layer (Shibata & Tanuma 2001). In scenarios where multiple plasmoids are present in the current layer, they can merge or separate as they propagate toward the current sheet exhausts, the termination regions of the main current sheet, and trigger higher levels of plasmoid instability until their sizes approach the electron and ion kinetic scale of the current sheet plasma (Kliem et al. 2000; Shibata & Tanuma 2001). This tearing of the current and merging of plasmoids allows magnetic reconnection to occur in bursts. In an attempt to link current observation capabilities to current sheet processes, recent magnetohydrodynamic (MHD) simulations of solar flares by Wyper & Pontin (2021) and Dahlin et al. (2025) have shown that current sheet plasmoids produced by the plasmoid instability map into the chromosphere as swirls and wave-like features along the flare ribbon fronts. In both studies, the appearance of ribbon features is more prevalent for the oblique tearing modes (Daughton et al. 2011), which form plasmoids at an oblique angle to the guide field.

Although there are no direct magnetic measurements of coronal plasmoids, many observations are interpreted as plasmoid signatures. In the chromospheric and corona, bright blob-like features have been interpreted as evidence of current sheet plasmoids (Ohyama & Shibata 1998; Kliem et al. 2000; Takasao et al. 2012; Hayes et al. 2019; Lu et al. 2022; Kumar et al. 2025). Furthermore, new adaptive optics systems on the Goode Solar Telescope (GST; Goode et al. 2010; Schmidt et al. 2018) have resolved the dynamical evolution of one such coronal structure in a post-reconnection magnetic loop system (Schmidt et al. 2025).

Plasmoid instability has been also reported in the context of magnetic reconnection in different plasma environments. It has been identified as a candidate to produce substructures small-scale spiral features in Earth's aurora (Huang et al. 2022; Nakamura et al. 2025). In the astrophysical context, plasmoid instability has been linked to substructure observations in numerical experiments of pulsar winds (Cerutti & Giacinti 2021), accretion disks of black holes (Ripperda et al. 2022) and multiphase interstellar wind (Fielding et al. 2023). Plasmoids have also been observed in magnetic reconnection laboratory experiments with collisionless (Olson et al. 2016) and collisional-collisionless (Zhao et al. 2022) plasma regimes. Therefore, the study of flare ribbon morphology substructure in the context of reconnection events should provide new perspectives into coronal current sheet reconnection physics.

In two-ribbon solar flares the coronal magnetic reconnection dynamics can be approximated by combining measurements of the photospheric magnetic field and flare ribbon morphology evolution. Forbes & Lin (2000) described the breakdown of the *frozen flux* condition (Alfvén 1942), consistent with the general theory of 3D magnetic reconnection

(Hesse & Schindler 1988; Schindler et al. 1988; Hesse et al. 2005; Wyper & Hesse 2015), as

$$\frac{d\Phi}{dt} = - \int \int_A (\nabla \times \mathbf{R}^{\text{cor}})_{\parallel} dA = \oint_{\mathcal{M}(\mathcal{B}(t))} \mathbf{B}_n^{\text{phot}} \frac{d\mathcal{B}}{dt} dl. \quad (1)$$

Here $d\Phi/dt$ represents the reconnection flux rate, $(\nabla \times \mathbf{R}^{\text{cor}})_{\parallel}$ the curl of the non-ideal coronal electric-field (\mathbf{R}^{cor}) parallel to the local magnetic field vector, $\mathcal{M}(\mathcal{B}(t))$ is the cumulative ribbon area boundary, $d\mathcal{B}/dt$ the multi-spatial-scale flare ribbon morphology evolution rate, and $\mathbf{B}_n^{\text{phot}}$ the magnetic field normal to the solar surface. The reconnection flux rate ($d\Phi/dt$) represents the magnetic flux that changed connectivity due to the coronal magnetic reconnection process. This break in the *frozen flux* condition is described by $(\nabla \times \mathbf{R}^{\text{cor}})_{\parallel}$. The non-ideal coronal electric field is represented by the relevant terms of the generalized Ohm's law for coronal plasma (Somov 2006). In the coronal context, Ohm's law is often approximated by its resistive form, such that the non-ideal electric field is written as $\mathbf{R}^{\text{cor}} \approx \eta \mathbf{j}^{\text{cor}}$, where η denotes the plasma resistivity. However, this description does not require explicit knowledge of the physical origin of the non-ideal electric field. Instead, the coronal reconnection process can be approximated using lower atmospheric observations, as described on the right-hand side of Equation 1.

In this paper, we explore the relationship between the evolution of flare ribbon substructure and other indicators of coronal reconnection dynamics (e.g. ribbon-derived magnetic reconnection rates, HXR and ultraviolet (UV) emission, and non-thermal velocities derived from chromospheric and transition region emission). Additionally, we present a new methodology to characterize the spatial complexity of the flare ribbon based on a combination of the box-counting dimension and the generalized version of the correlation dimension mapping algorithm (Mason & Uritsky 2022). The paper is organized as follows. In Section 2 we describe the data used in this study and the new methodology to track the flare ribbons' bright leading edge and characterize their spatial complexity. In Section 3 we present our results from tracking the spatial and temporal evolution of flare ribbon substructure complexity for an M6.5 solar flare, and the comparison to other indicators of magnetic reconnection dynamics. In Section 4 we discuss and interpret our results in the context of recent works in the field. Finally, we summarize our findings in Section 5.

2. DATA & METHODS

2.1. Event & Data Description

In this section we describe observations from the Interface Region Imaging Spectrograph (IRIS; De Pontieu et al. 2014; De Pontieu et al. 2021), Helioseismic Magnetic Imager (HMI; Hoeksema et al. 2014) and Atmospheric Image Assembly (AIA; Lemen et al. 2012) onboard the Solar Dynamics Observatory (SDO; Pesnell et al. 2012), Fermi Gamma-ray Space Telescope (Fermi; Atwood et al. 2009), and Geostationary Operational Environmental Satellite (GOES; Bornmann et al. 1996; Chamberlin et al. 2009) that we use to analyze an eruptive M6.5 flare on 2015 June 22. From the GOES soft X-ray (SXR) lightcurve the flare starts at 17:39 UT in National Oceanic and Atmospheric Administration (NOAA) Active Region (AR) 12371 close to the solar disk center. The magnetic configuration of AR 12371 at the time of the flare is shown in the middle panel of the second row of Figure 1. Additionally, this figure highlights observations from 17:39 UT to 18:20 UT, capturing mostly the impulsive phase of the flare, where IRIS and AIA see the development and evolution of the flare ribbons.

We use the SDO AIA 1600 Å intensity maps and HMI magnetic field measurements to derive reconnection fluxes and reconnection rates as described in Equation 1. The 1600 Å intensity maps correspond to a characteristic temperature response of 5000 K and 10⁵ K, sensitive to chromospheric emission (mainly contain C IV doublet 1548.20 Å & 1550.77 Å, and continuum emission). AIA 1600 Å data has a spatial resolution of 0.6'' and cadence of 24 seconds. HMI vector magnetic field maps, which include the line-of-sight (LOS) field strength, inclination and azimuthal angles, are transformed into the vector magnetic field components in the local reference frame B_x , B_y , and B_z (Sun 2013; Bobra et al. 2021). The HMI magnetic field data has a 720 second cadence and 0.5'' pixel resolution (Kazachenko et al. 2017). In the local reference frame, B_z is the magnetic field component perpendicular to the active region solar surface. AIA observed the entire evolution of the flare ribbons within a full-disk field-of-view (FOV). The IRIS Slit-Jaw Imager (SJI) provides higher resolution images with 0.33'' spatial pixel resolution (almost twice that of AIA 1600 Å) and a cadence of 17 seconds in the 1330 Å passband within a limited FOV (the dashed green box in the AIA and HMI maps of Figure 1 shows the IRIS-SJI FOV). The 1330 Å SJI channel probes from coronal to chromospheric temperatures (10⁷ – 5000 K; which mainly contains C II doublet 1334 Å & 1335 Å, Fe XII 1349.4 Å, Fe XXI 1354.08 Å, and continuum emission) and reveals additional spatial structures of the flare ribbons.

To describe the non-thermal and high-energy flare properties, we use observations from the IRIS Spectrograph (SG), Fermi’s *Gamma-ray Burst Monitor* (GBM, Meegan et al. 2009), and GOES X-ray Sensor (XRS; Machol et al. 2019). IRIS-SG measures spectral profiles from multiple emission lines, including the Si IV 1402.77 Å transition region line. We fit a single Gaussian profile to the Si IV spectra to calculate intensity, Doppler velocity, and non-thermal velocity ($\nu_{\text{non-thermal}}$) within the raster region (blue rectangle in Figure 1) every 34 seconds. We use GBM’s Continuous Spectroscopy (CSPEC) data, downloaded with *OSPEX* IDL software⁹, to evaluate HXR temporal and spectral evolution during flares. The CSPEC data has a varying cadence from 1.0 seconds to 32.7 seconds, and a default value of 4.0 seconds, and is stored in 128 quasi-logarithmic energy bins, which can be integrated into the following energy channels of interest: 8 – 15 keV, 15 – 25 keV, 25 – 50 keV, 50 – 100 keV, and 100 – 300 keV. Finally, to measure flare lightcurves in soft X-ray (SXR), we use observations from GOES XRS with a cadence of 1 s in two channels, 0.5 – 4 Å and 1 – 8 Å, corresponding to an energy range between about 1.5 and 25 keV.

2.2. Tracking the Flare Ribbon Bright Leading Edge (FRBLE)

To describe the small-scale morphological changes of the ribbon in the plane-of-sky (POS), we decompose the intensity images from IRIS (I) into various features. Appendix B shows the intensity decomposition and feature extraction application to a synthetic image. This application to synthetic data illustrates the general usability of our feature extraction methodology to astrophysical image datasets. First, we distinguish flare-ribbon emission (I_{FR}^*) from background emitting plasma (I_{BG}^*). We use intensity decomposition on a logarithmic scale ($I^* = \log_{10}(I)$) to allow for a more easy visualization of high-contrast spatial features. Extracting the flare ribbon from the background emission can be achieved with many different methods (e.g., Yang et al. 2018; Kirk et al. 2013; Maurya & Ambastha 2010). We use the Qu et al. (2003); Qiu et al. (2004) intensity threshold method with

$$I^*(x_i, y_j, t_k) = \begin{cases} I_{\text{FR}}^*(x_i, y_j, t_k; \epsilon_{\text{FR}}) & \text{if } I^*(x_i, y_j, t_k) \in I^*(x_i, y_j, t_k) \mathcal{N}(x_i, y_j, t_k; c; \tau_{\text{FR}}; \epsilon_{\text{FR}}), \\ I_{\text{BG}}^*(x_i, y_j, t_k; \epsilon_{\text{FR}}) & \text{if } I^*(x_i, y_j, t_k) \notin I^*(x_i, y_j, t_k) \mathcal{N}(x_i, y_j, t_k; c; \tau_{\text{FR}}; \epsilon_{\text{FR}}). \end{cases} \quad (2)$$

Here we define an instantaneous threshold mask \mathcal{N} for position (x_i, y_j) at observation time t_k as

$$\mathcal{N}(x_i, y_j, t_k; c; \tau_{\text{FR}}; \epsilon_{\text{FR}}) = \begin{cases} 1 & \text{if } \bar{I}^*(x_i, y_j, t_k; \tau_{\text{FR}}) + \epsilon_{\text{FR}}(x_i, y_j, t_k; \tau_{\text{FR}}) \geq c * \tilde{I}^*, \\ 0 & \text{if } \bar{I}^*(x_i, y_j, t_k; \tau_{\text{FR}}) + \epsilon_{\text{FR}}(x_i, y_j, t_k; \tau_{\text{FR}}) < c * \tilde{I}^*. \end{cases} \quad (3)$$

In these equations \mathcal{N} discriminates among pixels above the constant c multiplied by the median intensity \tilde{I}^* for all observation frames. The value of c is empirically chosen so that \mathcal{N} best matches the spatial distribution of I_{FR}^* . Typical c values used for the 1330 Å and 1400 Å SJI channels are 8 on the linear scale and 1.7 on the logarithmic scale. The intensity at each point in the frame is substituted by the running-window temporally averaged intensity \bar{I}^* , where $\tau_{\text{FR}} = \pm 95$ s (10 consecutive IRIS-SJI frames) is the chosen temporal window. We choose $\tau_{\text{FR}} = \pm 95$ s empirically because it eliminates bright transients produced by heating episodes spatially uncorrelated to the flare ribbon emission while maintaining the original spatial distribution of the flare ribbons. Temporally averaging the intensity reduces the occurrence frequency of transient bright features contaminating the instantaneous flare ribbon mask. Errors in the masking procedure due to thresholding, transient bright structures, pixel saturation and bleeding, dust on top of the camera detector, pixel interpolation, and other sources are represented by the variable ϵ_{FR} . Yang et al. (2018) have indicated that this instantaneous flare ribbon masking method (\mathcal{N}) can overestimate the area enclosing the flare ribbon and, therefore, would fail to accurately track the morphological changes of the flare ribbon substructure. Furthermore, as discussed by Corchado Albelo et al. (2024), the cumulative mask (\mathcal{M}) indicates the first time a given pixel intensity $I(x_i, y_j, t_k)$ exceeds the chosen background threshold and thus corresponds to the first brightening of the flare ribbon at a given coordinate ($\mathcal{M}(x_i, y_j, t_k) = \mathcal{N}(x_i, y_j, t_k) \cup \mathcal{M}(x_i, y_j, t_{k-1})$). Moreover, substructures have been observed to develop in regions within the cumulative mask of the flare ribbon, making this method ill-suited for temporally tracking the substructure development on flare ribbon observations. Therefore, we modify the methodology of Qiu et al. (2004) to track the evolution of substructures, and limit the use of the cumulative ribbon mask method to calculate the reconnection flux and rate.

⁹ https://hesperia.gsfc.nasa.gov/fermi_solar/analyzing_fermi_gbm.htm

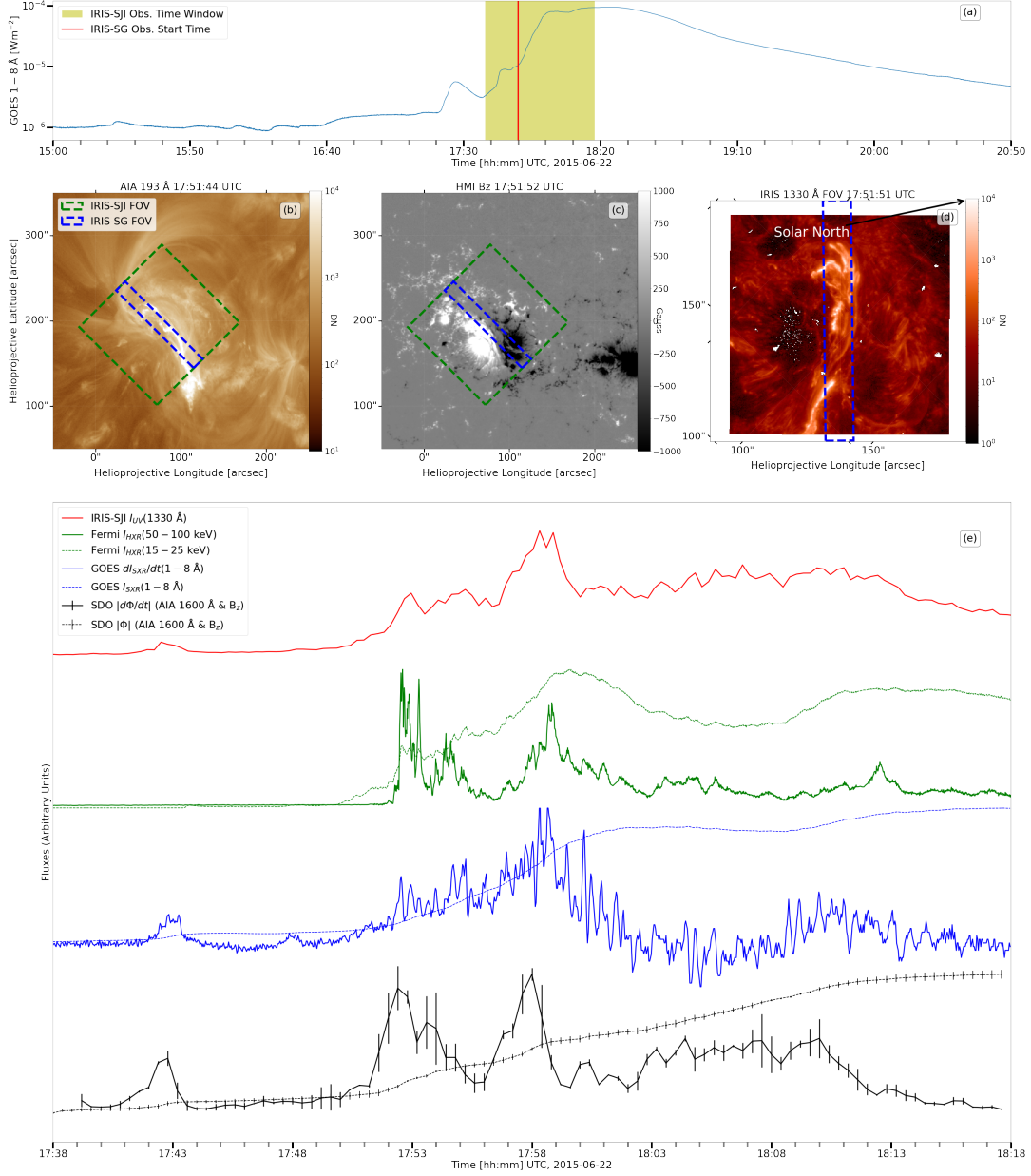


Figure 1. Overview of the M6.5 flare in AR 12371 on 2015 June 22. (a) GOES 1 – 8 Å light curve; the IRIS-SJI analysis window is shaded yellow and the IRIS-SG start time is marked by the vertical line. (b) AIA 193 Å image at 17:51 UT, (c) corresponding HMI B_z magnetogram at 17:51 UT; (d) IRIS-SJI 1330 Å at 17:51 UT. Green and blue boxes show the SJI and SG FOVs, respectively. (e) Normalized time series of variables integrated over respective field of views: IRIS 1330 Å intensity (I_{UV} ; red), GOES 1–8 Å (I_{SXR} ; blue dashed) and its time derivative (dI_{SXR}/dt ; blue solid), Fermi (I_{HXR}) 15–25 keV (green dashed) and 50–100 keV (green solid), and ribbon-derived reconnection flux (Φ ; black dashed) and rate ($d\Phi/dt$; black solid).

The substructure related to current sheet processes develops in the apparent interface between the leading edge and the rest of the flare ribbon body (Kerr et al. 2021; Naus et al. 2022; Polito et al. 2023; Kerr et al. 2024; Pietrow et al. 2024). We call this interface, which corresponds to the brightest region of the flare ribbons, the Flare Ribbon Bright Leading Edge (FRBLE). In the context of ultraviolet flare kernels observed in the IRIS-SJI channels (Kowalski et al. 2017), the FRBLE is the area enclosing all of the kernels. Furthermore, we use the cumulative area enclosed by the FRBLE to calculate the reconnected magnetic flux in observations

$$\Phi^\pm = \iint_{\mathcal{M}(\mathcal{B}_{\text{FRBLE}})} B_z^\pm dA_{\text{FRBLE}}, \quad (4)$$

from which we then take the derivative to find the reconnection flux rate (Kazachenko et al. 2017; Naus et al. 2022; Corchado Albelo et al. 2024). Trailing behind this region is the so-called flare ribbon moss, which forms a web-like structure of all cooling flare ribbon pixels (Fletcher & Hudson 2001). This moss region also has substructure, but is believed to arise from the energy dissipation in the lower atmospheric layers and therefore does not serve as a diagnostic of the flare current sheet conditions. To identify the spatial substructure, we decompose flare ribbons into moss and FRBLE areas:

$$I_{\text{FR}}^*(x_i, y_j, t_k; c) = \begin{cases} I_{\text{FRBLE}}^*(x_i, y_j, t_k; c; l) & \text{if } I_{\text{FR}}^*(x_i, y_j, t_k; c) \in I_{\text{FR}}^*(x_i, y_j, t_k; c)\mathcal{L}(x_i, y_j, t_k; c; l), \\ I_{\text{Moss}}^*(x_i, y_j, t_k; c; l) & \text{if } I_{\text{FR}}^*(x_i, y_j, t_k; c) \notin I_{\text{FR}}^*(x_i, y_j, t_k; c)\mathcal{L}(x_i, y_j, t_k; c; l), \end{cases} \quad (5)$$

where \mathcal{L} is a FRBLE mask

$$\mathcal{L}(x_i, y_j, t_k; c; l) = \begin{cases} 1 & \text{if } \mathcal{N}(x_i, y_j, t_k; c)\nabla^2(I^*(x_i, y_j, t_k)) \leq l, \\ 0 & \text{if } \mathcal{N}(x_i, y_j, t_k; c)\nabla^2(I^*(x_i, y_j, t_k)) > l. \end{cases} \quad (6)$$

Here we define the FRBLE region as the area with a negative second spatial derivative ($\nabla^2 I^*$), in the logarithmic scaled image, below a given threshold $l = -10^{-2}$ pixel $^{-2}$. We use the Laplacian of Gaussian (LoG) filter from the Python Scipy image processing package (Virtanen et al. 2020; Marr & Hildreth 1980) to estimate $\nabla^2 I^*$. The LoG operator has been used by Gill et al. (2010) to detect the flare ribbon leading edges on AIA 1600 Å observations. We use a standard deviation of $\sigma = 2.5$ pixels ≈ 0.603 Mm to define the Gaussian function used to reduce the noise in the $\nabla^2 I^*$ calculation while avoiding degrading substructures.

Finally, since the extracted mask can include small artifacts, we clean the extracted mask. We eliminate the small bright artifacts, arising from numerical noise and transient brightening in the 1300 Å channel, by imposing that the length (\mathcal{P}) of each \mathcal{L} segment be greater than 10% of the largest segment. Afterwards, we use the clean FRBLE binary image to extract the boundary $\mathcal{B}_{\text{FRBLE}}(x_i, y_j, t_k; c; l)$, using the OpenCV Python package (Bradski 2000). We then used $\mathcal{B}_{\text{FRBLE}}$ to infer the spatial complexity along the FRBLE and track the substructures of interest.

2.3. Quantifying the Spatial Complexity of Flare Ribbon Substructure

Flare ribbon substructures that have been linked to coronal plasmoids (e.g., swirls and wave-like features) can be mathematically described as small-scale morphological variations of the FRBLE boundary, $\mathcal{B}_{\text{FRBLE}}$. Therefore, to track the development and evolution of the flare ribbon substructure, we seek a metric that quantifies the morphological complexity of the boundary across multiple spatial scales. Appendix C and Figure 2 of Mason & Uritsky (2022) show application of such morphology complexity metric to curvilinear and multi-scale boundaries. These tests and example figures illustrate the general applicability of the metrics and its sensitivity to the selected range of spatial scales.

Flare ribbons often exhibit complex large-scale curvilinear morphology (e.g. *J-shaped* flare ribbon hooks; Janvier et al. 2016), caused by the formation of newly reconnected loops and the global magnetic topology described by the three-dimensional standard flare model (Longcope et al. 2007; Aulanier et al. 2013; Janvier et al. 2013). To isolate the complexity changes associated with flare-ribbon substructure evolution and potential diagnostic of current-sheet fragmentation, we restrict our analysis to spatial scales smaller than those characterizing the large-scale ribbon morphology. Furthermore, since flare ribbons in observations are not inherently contiguous structures, and numerical noise may introduce artificial fragmentation in \mathcal{L} , each ribbon segment is analyzed separately to measure local spatial complexity along $\mathcal{B}_{\text{FRBLE}}$. For this purpose, we use the spatially dependent correlation integral ($C(r, x, y)$; Grassberger & Procaccia 1983) to perform Correlation Dimension Mapping (CDM), following Mason & Uritsky (2022):

$$C(r, x, y, t) = \sum_{i=1}^{N(x, y, t)} \Theta \left(r - \sqrt{(x_i - x)^2 + (y_i - y)^2} \right), \quad (7)$$

$$C(r, x, y, t) \sim r^{\mathcal{D}(x, y, t)}. \quad (8)$$

Here C is the spatially dependent correlation integral (Grassberger & Procaccia 1983), Θ is the Heaviside function (Heaviside 2011, defined as 1 when its argument is positive and 0 otherwise), r is the spatial scale of interest, and N is the number of points along the boundary within the maximum radial scale $r_{\text{max}} = \max(r)$, at time t . The

spatially dependent correlation dimension $\mathcal{D}(x, y, t)$ is obtained by fitting a linear relation to the log–log dependence of $C(r, x, y, t)$ on r over the range $[r_{\min}, r_{\max}]$.

To characterize the overall complexity of the FRBLE boundary, we define a weighted mean correlation dimension,

$$\bar{\mathcal{D}} = \sum_i^{N_{\text{FRBLE}}} \mathcal{D}_i w_{\mathcal{D}}, \quad (9)$$

where $w_{\mathcal{D}} = N_{\mathcal{D}}/N_{\text{FRBLE}}$ represents the fraction of boundary points with correlation dimension \mathcal{D} , and $N_{\mathcal{D}}$ is the total number of points along the FRBLE boundary.

The correlation dimension is conceptually related to the Minkowski–Bouligand dimension (Minkowski 1901; Bouligand 1929), more commonly referred to as the **box-counting dimension** ($\mathcal{D}_{\text{BC}}(N, \varepsilon, t)$), of a binary image. The box-counting dimension is defined as

$$\mathcal{D}_{\text{BC}}(N, \varepsilon, t) = - \lim_{\varepsilon \rightarrow 0} \frac{\log N(\varepsilon, t)}{\log \varepsilon}, \quad (10)$$

where $N(\varepsilon, t)$ denotes the number of boxes with linear size ε needed to cover the area of a binary object at time t . A fractional value of \mathcal{D}_{BC} describes the global fractal, or space filling properties of the object’s boundary.

Importantly, the box-counting dimension \mathcal{D}_{BC} provides a global measure of spatial complexity and does not resolve localized variations along the FRBLE boundary $\mathcal{B}_{\text{FRBLE}}$ that are used to track substructure evolution. In our application, \mathcal{D}_{BC} describes the overall FRBLE’s global spatial-complexity at each magnetic polarity, incorporating the full spatial extent of the boundary morphology.

In contrast to the box-counting method, the CDM method provides a spatially-localized complexity value at each boundary point \mathcal{D} , computed over a neighborhood determined by the selected scale range. This enables the identification of specific regions along the FRBLE potentially impacted by the flare reconnection dynamics. Furthermore, unlike standard box-counting, CDM can be applied to any type of boundary that is non-fractal, fractal, or multi-fractal in nature.

3. RESULTS

In this section, we apply the Flare Ribbon Bright Leading Edge (FRBLE) tracking algorithm to IRIS 1330 Å SJI data of the 2015 June 22 M6.5 flare and quantify the spatial complexity of the evolving ribbon structure using the Correlation Dimension Mapping (CDM) and Box-Counting Dimension.

3.1. Spatial Evolution of Flare Ribbon Substructure Complexity

Figure 2 shows the extracted FRBLE at different stages of the flare impulsive phase (Figure 1(a) SXR light curve). The middle red column highlights the different stages of the 1330 Å emission: (a5) onset of the rapid increase ($t \approx 17:52$ UT), (b5) the peak ($t \approx 17:58$ UT), and the decay ($t \approx 18:16$ UT). The IRIS slit-jaw imager (SJI) FOV captures the full evolution of the northernmost ribbon, mostly embedded in the positive vertical magnetic field polarity (see Figure 1). However, the southernmost ribbon, associated with the negative polarity, is only partially captured within the IRIS-SJI FOV, representing a limitation of our analysis. The missing segment of the southernmost ribbon corresponds primarily to the *J-shaped* hook structure of the negative magnetic polarity. Such hook structures are generally interpreted as the chromospheric footpoints of the erupting flux rope (e.g. Démoulin et al. 1996; Janvier et al. 2013, 2016; Savcheva et al. 2012, 2015, 2016). This interpretation is consistent with observations of a halo CME (Gopalswamy et al. 2018) associated with this M6.5 flare.

As seen in Figure 2, fine substructure develops through the entire extent of the observed flare ribbon. This behavior is qualitatively consistent with theoretical interpretations in which the FRBLE substructure reflects the properties of the three-dimensional reconnection current sheet (Wyper & Pontin 2021; Dahlin et al. 2025). The incomplete coverage of the negative-polarity hook therefore suggests that our analysis may underestimate the substructures associated with magnetic field lines rooted in the erupting flux rope’s topological domain. Nevertheless, high-spatial resolution observations of two-flare-ribbons rarely capture the full spatial extent of the ribbon kernels in both B_z polarities. Even with partial coverage, our case study therefore represents a realistic application of the FRBLE tracking and CDM analysis, which can be systematically repeated for other high-resolution flare ribbon observations.

Throughout the impulsive phase of the flare, the FRBLE boundary exhibits a modest degree of fragmentation. This effect is most significant during the early and late stages of the impulsive phase (top and bottom rows of Figure 2).

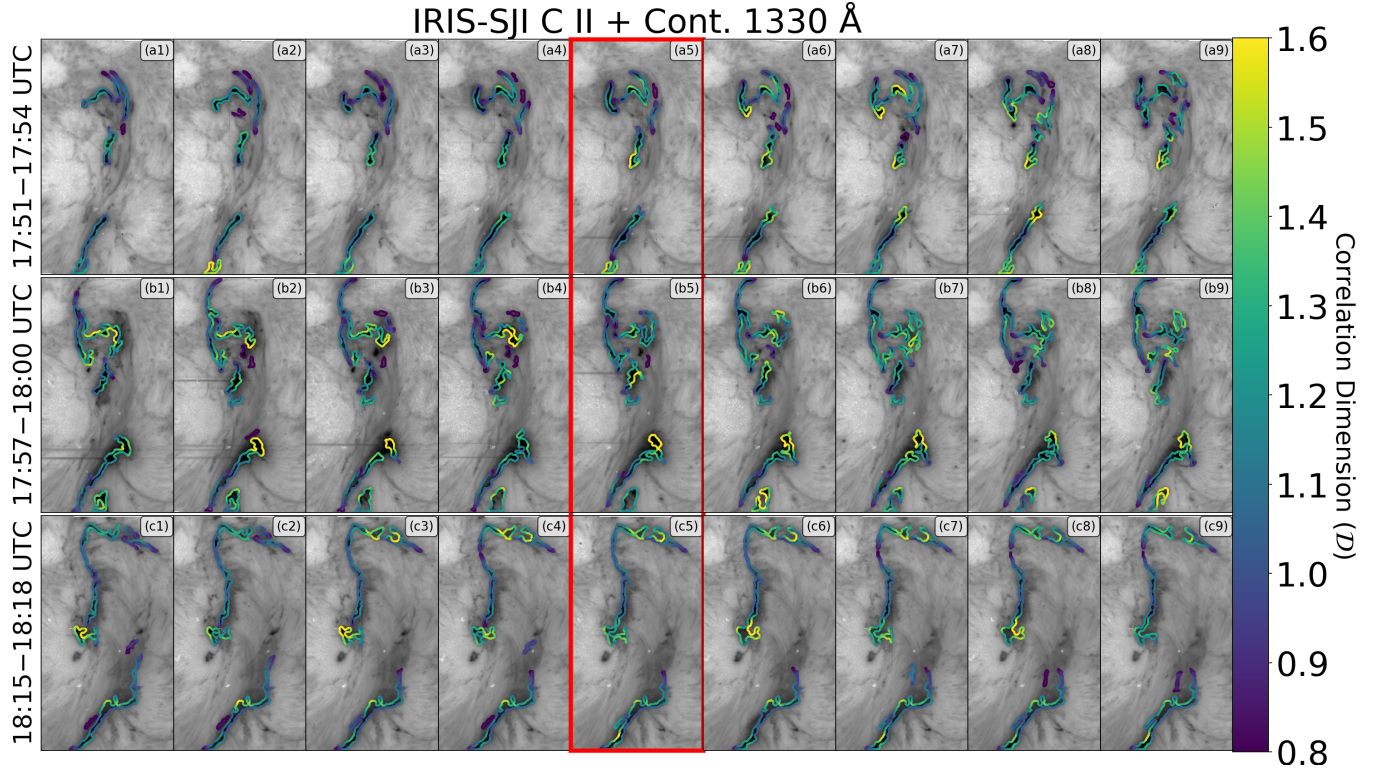


Figure 2. Spatial evolution of the FRBLE boundaries and local correlation dimension (\mathcal{D}) over IRIS 1330 Å SJI. Images are shown as \log_{10} intensity (I^* ; $1-10^4$ DN; reversed grayscale). Rows (a1-a9), (b1-b9) and (c1-c9) show nine consecutive IRIS frames, during 17:51–17:53 UT, 17:57–18:00 UT and 18:15–18:18 UT, respectively. Red boxes mark the middle frames: 17:52 UT (a5), 17:58 UT (b5), and 18:16 UT (c5). Colors show \mathcal{D} along the FRBLE: higher values (yellow; $\mathcal{D} > 1.5$) indicate more corrugated/complex segments, while lower values (blue/dark; $\mathcal{D} \leq 1$) indicate smoother segments.

Early in the impulsive phase ($17:38 \text{ UT} \lesssim t \lesssim 17:51 \text{ UT}$), the flare ribbons develop from a few compact bright kernels (somewhat indistinguishable from other transient bright features) into a more contiguous distribution of ribbon kernels. Toward the flare decay phase ($t \gtrsim 18:14 \text{ UT}$), the HXR emission in the 25 – 50 keV (see Figure 1) and microwave emission ranging from 4.43 – 16.9 GHz (see Figure 1 in Kuroda et al. 2018) both reach a stable minimum. At this later stage, the flare-ribbon kernels progressively fade, increasing the difficulty of separating FRBLE emission from background moss structures in the observations. The apparent fragmentation of the FRBLE boundary at these times is beyond the scope of this study. Instead, we focus on describing the fine-scale substructure along the leading edge segments, which are independently analyzed using the CDM (see Section 2.3).

For the spatial scales of the CDM procedure we use a range from a minimum radius of $3.327''$ (10 pixels ≈ 2.413 Mm) to a maximum radius of $4.991''$ (15 pixels ≈ 3.619 Mm). This range is constrained by the LoG operator used in the FRBLE extraction procedure. In particular, the lower limit is set by the Nyquist-Shannon sampling theorem ($r_{\min} = 4\sigma = 10$ pixels; Nyquist 1928; Shannon 1949). The upper limit of spatial scales is manually selected to capture the smallest corrugations along the boundary while minimizing the inclusion of larger curvilinear structures in the main ribbons. As shown in Figure 2, most of the FRBLE boundary exhibits a relatively low correlation dimension, with $1.0 \lesssim \mathcal{D} \lesssim 1.2$. Regions with the highest correlation dimension \mathcal{D} highlight areas where the FRBLE boundary is highly corrugated; such regions appear intermittently along the entire boundary. These localized enhancements in spatial complexity are short-lived, persisting for approximately $19 \text{ s} \lesssim \Delta t \lesssim 95 \text{ s}$ before decaying as the FRBLE becomes less spatially complex.

3.2. Temporal Evolution of Flare Ribbon Substructure Complexity

Although the spatial properties of individual high-complexity regions are of interest, in this study we focus primarily on the global evolution of FRBLE complexity. In Figure 3(a–c), we overview the spatial distribution of values of FRBLE complexity, described by \mathcal{D} , along the FRBLE boundary. The northern (top) ribbon spans the positive

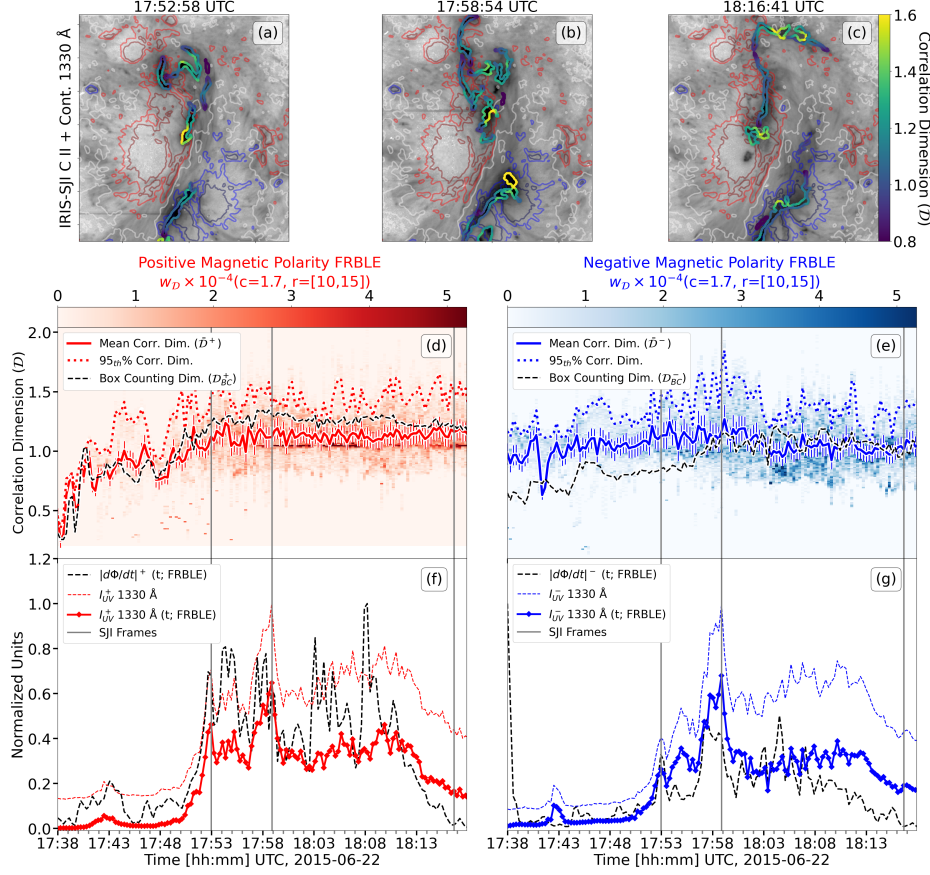


Figure 3. Evolution of FRBLE complexity and reconnection proxies. (a–c) Example frames (same as Fig. 2 a5, b5, c5) showing \mathcal{D} along the FRBLE at 17:52, 17:58, and 18:16 UT. Contours show HMI B_z levels: +500/+1000 G (red), –500/–1000 G (blue), and 0 G (white). (d,e) Distributions $w_{\mathcal{D}}$ for the positive and negative polarity ribbons. Solid lines show the mean $\bar{\mathcal{D}}$, dotted lines the 95th percentile, and black dashed lines the box-counting dimension \mathcal{D}_{BC} . (f,g) Time series reconnection dynamics proxies in positive and negative magnetic-polarity FRBLEs, respectively. The solid and dashed colored-lines (red and blue) represent the 1330 Å intensity emitted from the FRBLE and full SJI FOV respectively, while the black-dashed line shows the cumulative reconnection rate derived from FRBLE observations. Vertical gray lines mark the times in (a–c).

polarity footpoints of the newly formed flare arcade, whilst the southern (bottom) ribbon spans the negative polarity.

In Figures 3(d,e) we show the evolution of the statistical weight spatial complexity metric $w_{\mathcal{D}}$ separately within each magnetic field polarity. We analyze each polarity separately to determine whether observed trends in ribbon morphology correspond to similar reconnection processes in the current sheet. During the early impulsive phase at 17:38 UT – 17:48 UT, the positive-polarity FRBLE consists of a small number of compact kernels whose spatial extent is comparable to the CDM scale range. Because of the comparable CDM scale range and lack of well-developed substructure, $w_{\mathcal{D}}$ at these times concentrates in the positive polarity at lower correlation dimensions ($\mathcal{D} < 1$, see Appendix C for details). In contrast, the negative polarity FRBLE is larger compared to the CDM spatial scales, and exhibits more complex features from onset, yielding correlation dimensions closer to unity ($\mathcal{D} \approx 1$). The overall evolution of $w_{\mathcal{D}}$ in both polarity ribbons is well represented by the mean correlation dimension ($\bar{\mathcal{D}}$), which we adopt as the primary metric describing global complexity evolution. To track the most spatially complex regions, we use the 95th percentile of $w_{\mathcal{D}}$ (dotted lines in Figures 3(d,e)). High-complexity regions ($\mathcal{D} > 1.1$) in the positive polarity at this early stage temporally coincide with a small burst in the reconnection rate and intensity enclosed within the FRBLE.

Beginning around 17:53 UT, both polarities show a shift of $w_{\mathcal{D}}$ toward higher spatial complexity ($\mathcal{D} > 1$). This interval corresponds to bursty emission observed in HXR, SXR, microwave wavelengths, together with peaks in the reconnection rates derived within FRBLE areas. These signatures were previously reported as multi-wavelength quasi-

periodic pulsations rooted in the FRBLE region (see Figure 2 & 6 of Kuroda et al. 2018). At times of local intensity maxima in the 1330 Å emission and reconnection rate (black dashed vertical lines), small but systematic increases in \bar{D} are observed, driven by enhanced high-percentile complexity.

After around 18:00 UT, both the reconnection rate and 1330 Å emission decrease significantly, accompanied by a modest decline in FRBLE complexity. This level of complexity is maintained even as the flare approaches the decay phase, and the length of the FRBLE begins to decrease (Figure 3(c)). To quantify this relationship, we compute Spearman rank correlation coefficients between the reconnection flux rate and the mean correlation dimension in positive and negative B_z polarities (Spearman 1904). We find that the correlation coefficient is moderate: $r_S(|d\Phi/dt|^\pm, \bar{D}^\pm) = \{0.4, 0.3\}$, in positive and negative B_z polarities, respectively (Spearman 1904).

In Figure 4 we compare the box-counting dimension with FRBLE-derived reconnection flux rate in both polarities, from $\sim 17:43$ UT to $\sim 18:13$ UT, finding a power law relationship between the two: $|d\Phi/dt|^+ \propto \mathcal{D}_{\text{BC}}^{4.6 \pm 0.2}$ and $|d\Phi/dt|^- \propto \mathcal{D}_{\text{BC}}^{4.3 \pm 0.4}$. Furthermore, we find a strong correlation between the temporal evolution of box-counting dimension in the two polarities ($r_S(|d\Phi/dt|^\pm, \mathcal{D}_{\text{BC}}^\pm) = 0.7$).

As an independent test of the relationship between ribbon substructure and reconnection dynamics, in Figure 5, we compare the evolution of the mean non-thermal velocity $\bar{\nu}_{\text{non-thermal}}(t)$ with the mean correlation dimension of the FRBLE $\bar{D}(t)$. Each data point is recorded at the mean time of the 16 slit scans (every 34 seconds) composing each raster image. Importantly, the start time of Figure 5 is a subsample of the entire time series, starting when the FRBLE region first appears in the slit-raster region at $t \approx 17:50$ UT. At early times, the non-thermal velocity peaks in both the positive (35 km s^{-1} at $t \approx 17:52$ UT) and negative (48 km s^{-1} at $t \approx 17:55$ UT) polarity ribbons, coinciding with the increase in 1330 Å emission and the onset of bursty reconnection rates in both ribbons (Figure 3). After $t \approx 18:01$ UT, both ribbons show a decrease in non-thermal velocities, followed by a final burst around 18:12 UT. We find a moderate correlation between the mean correlation dimension and non-thermal velocity within the negative FRBLE within the IRIS-SG observed region ($r_S(\bar{D}^-, \nu_{\text{non-thermal}}^-) = 0.4$). In contrast, in the positive polarity IRIS-SG region, we find no significant monotonic correlation ($r_S(\bar{D}^+, \nu_{\text{non-thermal}}^+) = -0.2$).

4. DISCUSSION

In this study, we track the multi-spatial scale evolution of the flare ribbon leading edge boundary (FRBLE) and evaluate its relationship to observational proxies of magnetic reconnection processes. Our working hypothesis is that FRBLE boundary complexity reflects the underlying reconnection dynamics (Appendix A; Forbes & Priest 1984; Forbes & Lin 2000).

Using the box-counting dimension, we first quantify the *global* multi-scale morphology of the FRBLE. We find a strong monotonic correlation between the box-counting dimension and the reconnection flux rate in each magnetic polarity

$$r_S(|d\Phi/dt|^\pm, \mathcal{D}_{\text{BC}}^\pm) = \{0.7, 0.7\} \quad (11)$$

during $17:43 \text{ UT} \lesssim t \lesssim 18:13 \text{ UT}$). During the same time range, the two variables exhibit a power law relationship

$$d\Phi/dt \propto \mathcal{D}_{\text{BC}}^\gamma, \quad (12)$$

(see Figure 4). From cross-correlation analysis we find that reconnection flux rate lags the box-counting dimension by one time step (approximately 17 s, averaged across polarities). Given the cadence and uncertainties associated with computing the temporal derivative of magnetic flux, this delay is consistent with near co-temporal behavior, suggesting that the multi-spatial-scale ribbon morphology closely tracks reconnection dynamics.

In Appendix A we interpret the relationship between box-counting dimension and the magnetic reconnection flux rate (see Figure 4) approximated from FRBLE evolution as evidence of a fragmented current sheet. One mechanism that links the multi-spatial-scale nature of the FRBLE boundary to a fragmented coronal current sheet is the 3D oblique plasmoid instability (Wyper & Pontin 2021; Dahlin et al. 2025). With a parameterized analytical model Wyper & Pontin (2021) recently found that current sheet plasmoids (sunward and anti-sunward) trace to sub-scale deformations (wrappings, swirls, wave-like structures) along the flare ribbons. This result has been validated by Dahlin et al. (2025) using the Adaptively Refined Magnetohydrodynamics Solver (ARMS; DeVore & Antiochos 2008). However, these models do not include physical treatment of the particle energy gained due to non-thermal processes (Drake et al. 2006, 2010; Guidoni et al. 2016; Dahlin et al. 2017; Huang et al. 2017; Guidoni et al. 2022), nor the energy transport

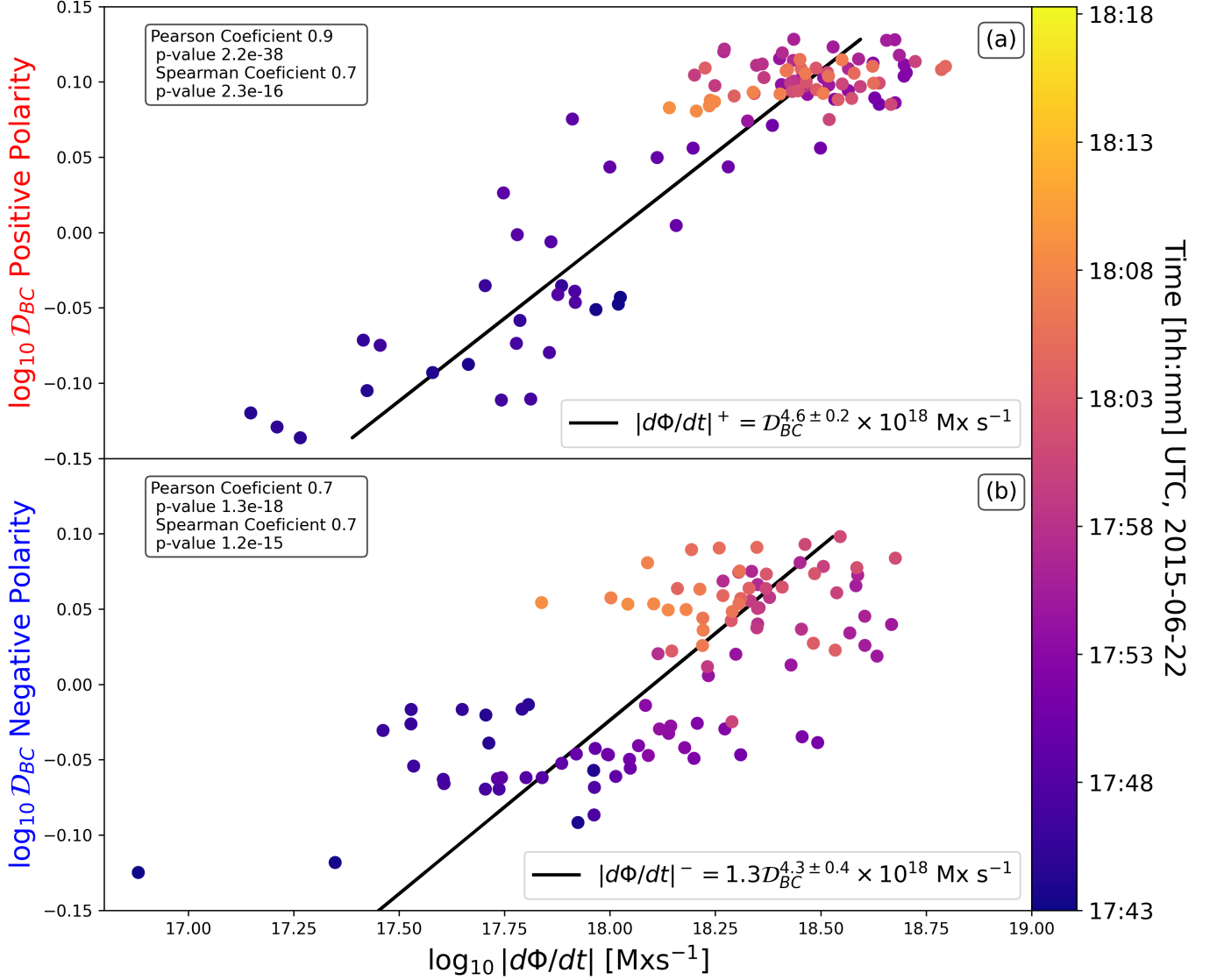


Figure 4. Reconnection rate vs. box-counting dimension. Absolute reconnection flux rate $|d\Phi/dt|$ versus box-counting dimension D_{BC} for the (a) positive and (b) negative polarity FRBLEs. Dots’ color encodes time (from $\sim 17:43$ UT to $\sim 18:13$ UT). Pearson and Spearman coefficients are listed in each panel. Best-fit power-law scales are shown in the lower right of each panel.

that gives rise to flare ribbon emission (Ramaty & Mandzhavidze 2000; Fletcher & Hudson 2008; Brosius 2012; Reep & Russell 2016; Polito et al. 2023). Regardless, the dynamics (and presence) of plasmoids in these 3D simulation results in a multi-spatial-scale flare leading edge boundary. Another fragmented current sheet scenario recently proposed is turbulent 3D reconnection (Wang et al. 2023, 2025). In these 3D simulations the turbulent current sheet breaks up into multi-spatial scale reconnection kernels, with spatial-scale-invariant reconnection rates. While our observational analysis suggests that magnetic reconnection occurs in a fragmented current sheet during this M-class flare (2015-06-22), it cannot distinguish the underlying physical details of the reconnection (e.g. plasmoid mediated reconnection, turbulent reconnection).

We then examine *localized* ribbon substructure using the correlation dimension metric (CDM, Mason & Uritsky 2022). Our CDM analysis shows that high-complexity regions are spatially localized and short-lived, persisting for approximately $19 \text{ s} \lesssim \Delta t \lesssim 95 \text{ s}$ after which they disperse or smooth at the analyzed substructure scales (2.4 - 3.6

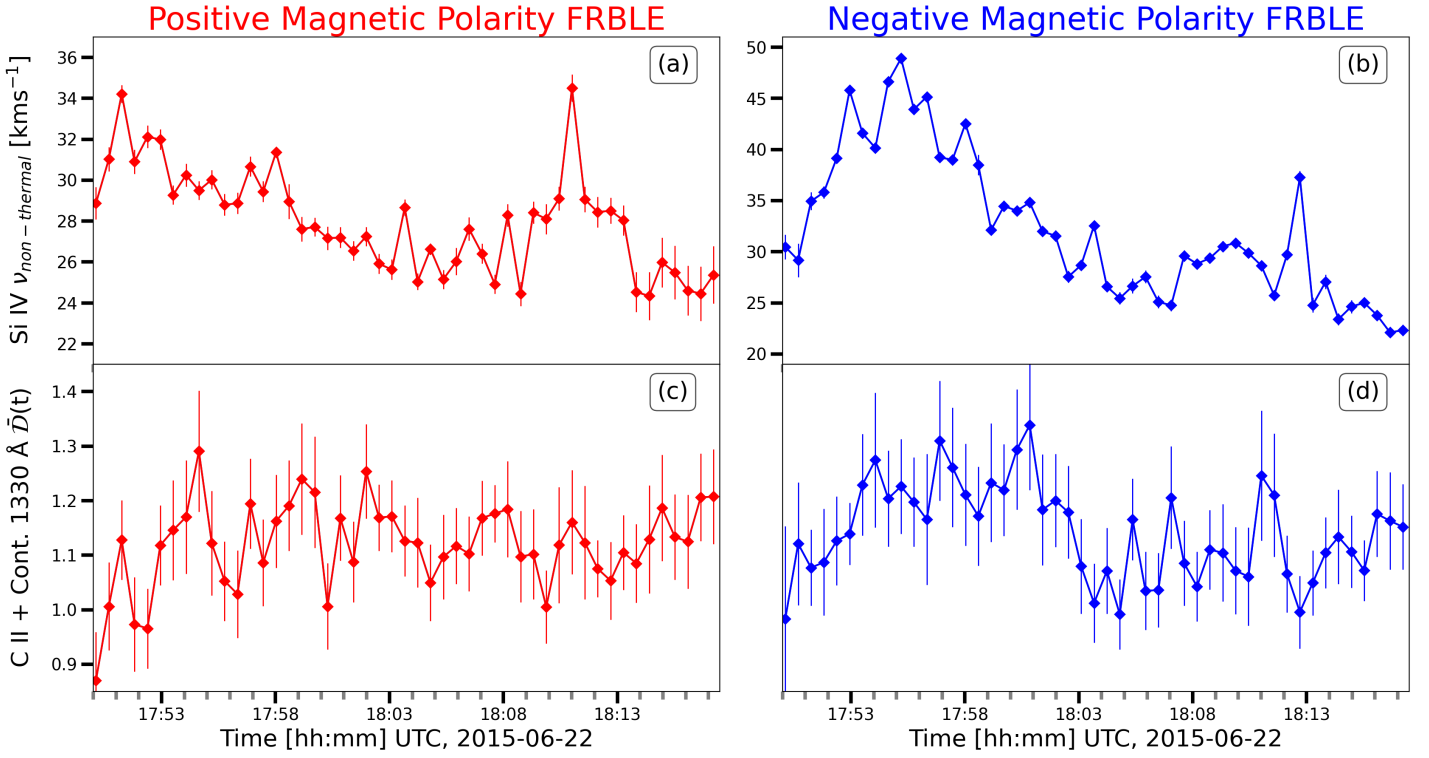


Figure 5. Mean non-thermal velocity vs. mean FRBLE complexity within the IRIS-SG raster region. (a,b) Mean Si IV non-thermal velocity $\bar{\nu}_{\text{non-thermal}}$ in the positive (red) and negative (blue) polarity FRBLE regions inside the raster region (blue rectangle in Fig. 1). (c,d) Corresponding mean correlation dimension \bar{D} for the same regions and color scheme.

Mm). We find that the mean CDM complexity metric along each magnetic polarity FRBLE exhibits a moderate correlation with the corresponding reconnection rate ($r_S(|d\Phi/dt|^\pm, \bar{D}^\pm) = \{0.4, 0.3\}$) (see Figure 3) and precedes it by approximately seven time steps (~ 119 s). This temporal offset and moderate correlation suggests that localized substructure evolution may not directly trace instantaneous reconnection rate variations.

To further explore this possibility, we compare the LOS non-thermal velocity with the evolution of the CDM complexity metric measured on the POS. In the negative-polarity ribbon within the IRIS-SG region, we find a moderate correlation: $r_S(\bar{D}^-, \nu_{\text{non-thermal}}^-) = 0.4$. No significant monotonic correlation is found for the positive polarity ribbon. Cho et al. (2024) describes the non-thermal velocity as the cumulative effect of multi-component plasma motions (beyond that explained by local thermodynamic motions of the plasma) along the LOS direction. Although some numerical experiments show that Si IV emission can be impacted by optical-depth effects (Kerr et al. 2019) it is usually characterized as optically thin plasma. Under the optically thin assumption the Si IV 1402.77 Å non-thermal velocity signatures are usually interpreted as being generated by turbulence. This turbulence has been reported to be generated by the interaction of waves (e.g. Jeffrey et al. 2018) across a wide spectrum of frequencies (broadband wave interaction) or the plasmoid instability (French et al. 2021). Following this interpretation, the mean degree of complexity examined in this work (\bar{D}) may represent the POS manifestation of macroscopic effects of turbulence, while the non-thermal velocity provides the LOS proxy of the same underlying plasma dynamics. Together, these measurements could inform us of a volumetric measure of the degree of turbulence in the lower atmospheric layers. Importantly, such an interpretation may explain the moderate correlation between the reconnection rates and the mean correlation dimension: $r_S(|d\Phi/dt|^\pm, \bar{D}^\pm) = \{0.4, 0.3\}$ (SJI observations in Figure 3). Footpoints of newly reconnected field lines could be heated and swirled continuously due to turbulent motions and dissipation over timescales that differ from the larger bursts observed in the reconnection rates, 1330 Å, and 50 – 100 keV HXR emission, which would correspond to non-thermal particle injection episodes.

Other potential contributions to the lack of strong correlation between the CDM complexity metric and indicators of reconnection dynamics are discussed below. First, the reconnection flux rate measure must be modified following the results of Wyper & Hesse (2015), to ensure that the evolution of the substructure complexity can be linked to the

reconnection dynamics associated with current sheet plasmoid, which is outside the scope of this project. Additionally, one could also expect mechanisms such as the apparent slipping motion of magnetic fields within a quasi-separatrix layer (Priest & Forbes 1992; Priest & Démoulin 1995) to be relevant in the evolution of the flare ribbon intensity substructure (Li & Zhang 2015; Purkhart et al. 2025). Additionally, slipping reconnection has also been associated with Si IV non-thermal velocity enhancements (Lörinčík et al. 2022), and flare ribbon co-spatial HXR sources (Purkhart et al. 2025) in previous observations. Another feasible contributor to the complexity of flare ribbon emission is the transmission of trapped non-thermal particles and heat fronts from the above-the-loop-top (ALT) region into the lower atmospheric layers. Recent studies have shown that the ALT region can host a variety of dynamical processes including multiple termination shocks (Shibata et al. 2023; Chen et al. 2015; French et al. 2024b), plasma instabilities (Shen et al. 2022), turbulence (Shen et al. 2023; Ashfield et al. 2024; Bacchini et al. 2024; Xie et al. 2025; French et al. 2024a), magnetic traps (Chen et al. 2024), and secondary reconnection episodes (Kołomański & Karlický 2007; Milligan et al. 2010; Kong et al. 2020). All of these processes could contribute to the continual energy gains of charged particles. Recently, a 3D flare model has shown that electrons escaping the ALT can generate HXR signatures in flare ribbons (Li et al. 2025). Our results do not allow us to distinguish between these relative contributions to the flare ribbon substructure evolution.

Altogether, our analysis is a first step towards quantitative linking of flare ribbon morphology to reconnection dynamics. We find that the box-counting dimension appears to provide a useful observational diagnostic of multi-scale reconnection behavior, while the CDM metric offers complementary insight into localized ribbon structure. Higher-resolution observations with instruments like the Daniel K. Inouye Solar Telescope (DKIST; Rimmele et al. 2020), and coordinated on-disk and off-limb observations of flares with the Solar Orbiter (Müller et al. 2020), will provide further evidence to understand the exact physical mechanism(s) dominating the evolution of flare ribbon substructures. Other advances in flare modeling like kglobal (Drake et al. 2019; Arnold et al. 2019; Drake et al. 2025) will allow for a more self-consistent development of non-thermal particle populations during flares at macro-scales (e.g. plasmoids). Additionally, MPI-AMRVAC (Keppens et al. 2012; Druett et al. 2023, 2024) flare experiments have made significant advances to the self-consistent treatment of multi-dimensional energy transport during flares and its impact on the lower solar atmosphere. These advances would be crucial to understanding the diagnostic potential of multi-scale, temporally- and spatially-variable flare ribbon observations.

5. CONCLUSIONS

In this paper, we introduce a new method for measuring the multi-spatial scale flare ribbon structure based on object extraction techniques, box-counting dimension, and correlation dimension mapping. We first test our methodology on synthetic datasets (Appendix B and C). We then apply the methodology to impulsive phase high-resolution and high-cadence IRIS observations of an M-class flare. Our findings are summarized as follows:

- We find a strong statistical correlation and power law relationship between the reconnection flux rate and the box-counting dimension of the flare ribbon. This result suggests that reconnection layers are spatially fragmented and dynamical (Forbes & Lin 2000). These results are consistent with earlier observations (e.g. Nakariakov & Melnikov 2009; Cannon et al. 2023; Collier et al. 2024; Corchado Albelo et al. 2024; Purkhart et al. 2025) and 3D flare simulations (e.g. Wyper & Pontin 2021; Wang et al. 2023; Dahlin et al. 2025; Wang et al. 2025).
- We find that high spatial complexity substructures ($\mathcal{D} \gtrsim 1.3$) are localized in time and space and disappear quickly (within 19 – 95 seconds or 1 – 5 IRIS-SJI frames) from the observations. Our temporal analysis of the mean FRBLE substructure complexity in each magnetic polarity shows that most of the enhancements in spatial complexity (bursts traced by the 95th percentile of the histogram in Figure 3) are moderately statistically correlated with the reconnection flux rate (in both polarity ribbons) and the non-thermal velocities (in negative polarity ribbon) derived from the Si IV 1402.77 Å. These results suggest that the correlation dimension at small scales (measure of how deformed substructures are) is not directly linked to the global reconnection properties (e.g. reconnection flux rate, non-thermal velocities). Rather, in the context of this study, CDM is most useful for spatially identifying substructures that contribute to enhanced values of the box-counting dimension. Our results do not allow us to distinguish the physical origin of the evolution of the flare ribbon substructure (e.g., plasmoid evolution, slipping motions, ALT region transport, or turbulent motions in the flaring atmosphere).
- In summary, we find strong evidence to suggest that magnetic reconnection occurs in a fragmented current sheet during the impulsive phase of this M-class flare observed on 2015-06-22 (Wyper & Pontin 2021; Guidoni et al.

2022; Dahlin et al. 2025; Wang et al. 2025). Our analysis can be applied to other high-resolution flare ribbon observations to calculate the commonality of the fragmented current sheet scenario, and further validate the methodology. Additional tests of simulations are required to draw physical conclusions about the evolution of the smallest substructures characterized by the CDM procedure.

We acknowledge support from NASA ECIP NNH18ZDA001N, and NSF CAREER SPVKK1RC2MZ3 (MDK, MFCA). MFCA thanks Caroline Evans for the discussion of the Leibniz integral formalism. MFCA also thanks Dr. Judith T. Karpen for valuable discussion and manuscript revision. Support for this work is provided by the National Science Foundation through the DKIST Ambassadors program, administered by the National Solar Observatory and the Association of Universities for Research in Astronomy, Inc. RJF thanks support from the NASA HGI award 80NSSC25K7927. CAT acknowledges support from NSF grant number 2407850. VMU was partly supported by the SESDA subcontract agreement administered by ADNET.

APPENDIX

In this section, we first explore the physical implication of the power law relationship observed between $d\Phi/dt$ and \mathcal{D}_{BC} , show 2 examples of our methodology applied to synthetic data, and later review the expected improvements to these methods when using higher-resolution and high-cadence observations.

A. EVIDENCE OF THE MULTI-SCALE CURRENT SHEET

As described in Section 1, Equation 1 allows us to relate the magnetic reconnection flux rate, observed in the lower solar atmosphere, to the curl of the non-ideal coronal electric field $(\nabla \times \mathbf{R}^{\text{cor}})_{\parallel}$ which describes the reconnection physics. In our study, we have found that there is a power law relationship between the reconnection flux rate and the box-counting dimension (see Figure 4). The functional form can be written as $d\Phi/dt(N, \varepsilon, t) = m\mathcal{D}_{BC}^{\gamma}(N, \varepsilon, t)$, where m and γ are constants determined from power law fits, and the number N of boxes with spatial scale ε is used to describe the FRBLE box-counting dimension. The coronal area of integration in Equation 1 is arbitrary if it includes all of the non-ideal electric field terms related to the change of magnetic flux. We consider the case in which the enclosing area is a smooth constant flux surface in the corona that includes all the terms $(\nabla \times \mathbf{R}^{\text{cor}})_{\parallel}$. By substituting the power law relationship with the left-hand side of the Equation 1 we find that

$$m\mathcal{D}_{BC}^{\gamma}(N, \varepsilon, t) = - \int \int_A (\nabla \times \mathbf{R}^{\text{cor}})_{\parallel} dA, \quad (\text{A1})$$

implying that $(\nabla \times \mathbf{R}^{\text{cor}})_{\parallel} = \mathcal{F}(N, \varepsilon, t)$. This relationship suggests that the physics involved in the reconnection process must be described by a multi-spatial-scale function $\mathcal{F}(N, \varepsilon, t)$. Such multi-spatial-scale reconnection physics supports the fragmented or inhomogeneous current sheet scenarios (e.g. plasmoid-unstable or 3D-turbulent current sheets).

B. FRBLE PROCEDURE ON SYNTHETIC DATA

A test of the object extraction technique procedure (FRBLE) is shown in Figure 6. We start by creating a synthetic ring structure and place circular substructures around the circumference. We then add white and colored noise (signal $\approx f^{\beta}$) to the image so that it resembles solar observations. The top row shows how a high intensity threshold ($I \geq 10$ DN) is used to extract the ring and circle substructures. The rightmost column shows the extracted features, after applying the cleaning algorithm. The binary image (c) shows that the extraction based on a global intensity threshold overestimates the features of interest (ring and circle substructures). The overestimation of the features is likely due to the high level of noise contamination and low contrast between background and features. The bottom row shows the application of the threshold based on the intensity curvature of the image ($\nabla^2 I$). We approximate the intensity curvature using a LoG operator with a $\sigma = 10$ pixel for noise reduction in the spatial derivative calculations. The final binary image (f) shows that the substructure has been successfully extracted, after applying the curvature threshold $\nabla^2 I \leq -1 \times 10^{-3}$ DN/pixel² and the cleaning procedure.

C. CORRELATION DIMENSION MAPPING ON SYNTHETIC MULTI-SCALE BOUNDARY OBJECT

Another test applied to synthetic data shows (Figure 7) the implementation of the CDM algorithm. We define a multi-scale boundary, top row of the figure, using a combination of sinusoidal functions and Weierstrass functions

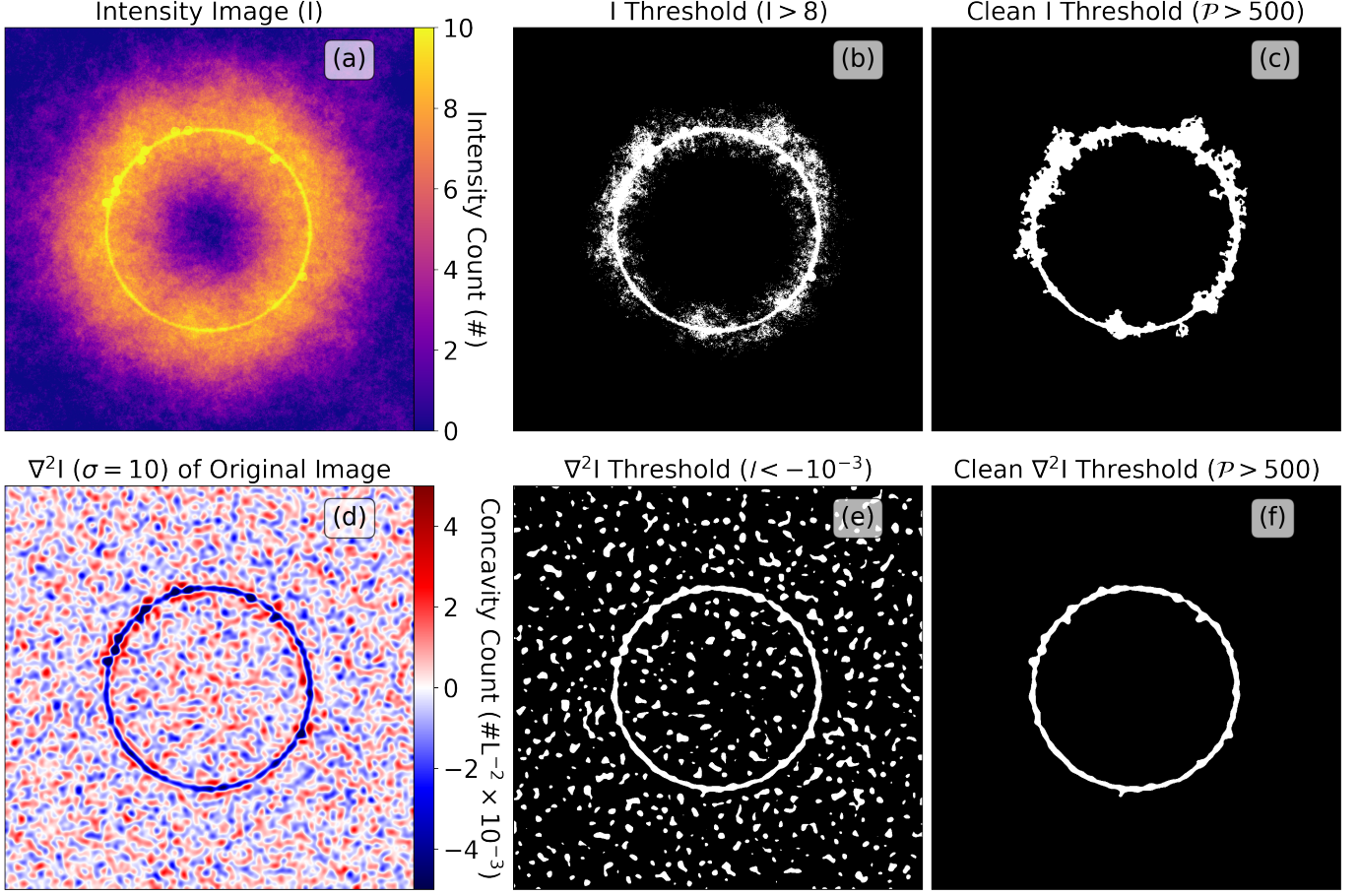


Figure 6. FRBLE extraction test on synthetic data. (a) Synthetic image: a ring with embedded circular substructures plus noise. (b,c) features extracted using a global intensity threshold, before and after cleaning. (d) Intensity curvature ($\nabla^2 I$) map. (e,f) Features extracted using a curvature threshold, before and after cleaning.

(Weierstraß 1988). The x and y coordinates of the boundary are defined as: $x = 1000 \cos(\pi t) + \sum_{i=0}^5 0.3^i \sin(23^i \pi t)$ and $y = 1000 \sin(\pi t) + \sum_{i=0}^5 0.3^i \cos(23^i \pi t)$. The box-counting dimension of this boundary is $\mathcal{D}_{BC} = 1.37 \pm 0.02$, which describes the multi-scale and space filling properties of the synthetic boundary. The bottom row highlights how the choice of r_{\max} in the CDM procedure determines the correlation dimension value \mathcal{D} and the location of high complexity regions. Overall, in regions where the boundary kinks the correlation dimension is higher, due to the substructure’s high spatial complexity (panels d and e). If the r_{\max} is comparable to the size of the main structure, CDM shows a more uniform spatial distribution and lower values of \mathcal{D} (panel e). However, when tuned to spatial scales of the same order of magnitude as the kinked or folded regions, the CDM map highlights these regions of varying complexity through higher localized values of \mathcal{D} (panel e). When using CDM, scales of known interest can be input *a priori*, or a series of tests with varying r ranges can be tested to extract the most relevant spatial scales for the data.

D. EXPECTED IMPROVEMENTS WITH HIGHER-RESOLUTION AND HIGHER-CADENCE DATA

It should be noted that the current implementation of the FRBLE tracking algorithm and CDM characterization of the substructure complexity are mainly dependent on two qualities of the dataset – the contrast between the FRBLE and the rest of the emitting atmosphere, and the spatial resolution of the observations. We employ spatial derivative filters on the IRIS intensity maps to circumvent the contrast between the FRBLE and the rest of the flare ribbon emission, which is extracted using intensity thresholds (Qiu et al. 2004; Mauitya & Ambastha 2010; Kirk et al. 2013; Yang et al. 2018). Yet, due to the sensitivity of the spatial derivatives to noise and pixel intensity saturation, we know that higher cadence (e.g. IRIS high-cadence program, Hi-C, MUSE, and SO-EUI) and higher spatial resolution (e.g. DKIST, GST, and SST) observations can provide a more accurate extraction of the flare ribbon substructure. Currently, to reduce potential artifacts (small scale morphology changes due to noise in the intensity maps) in the

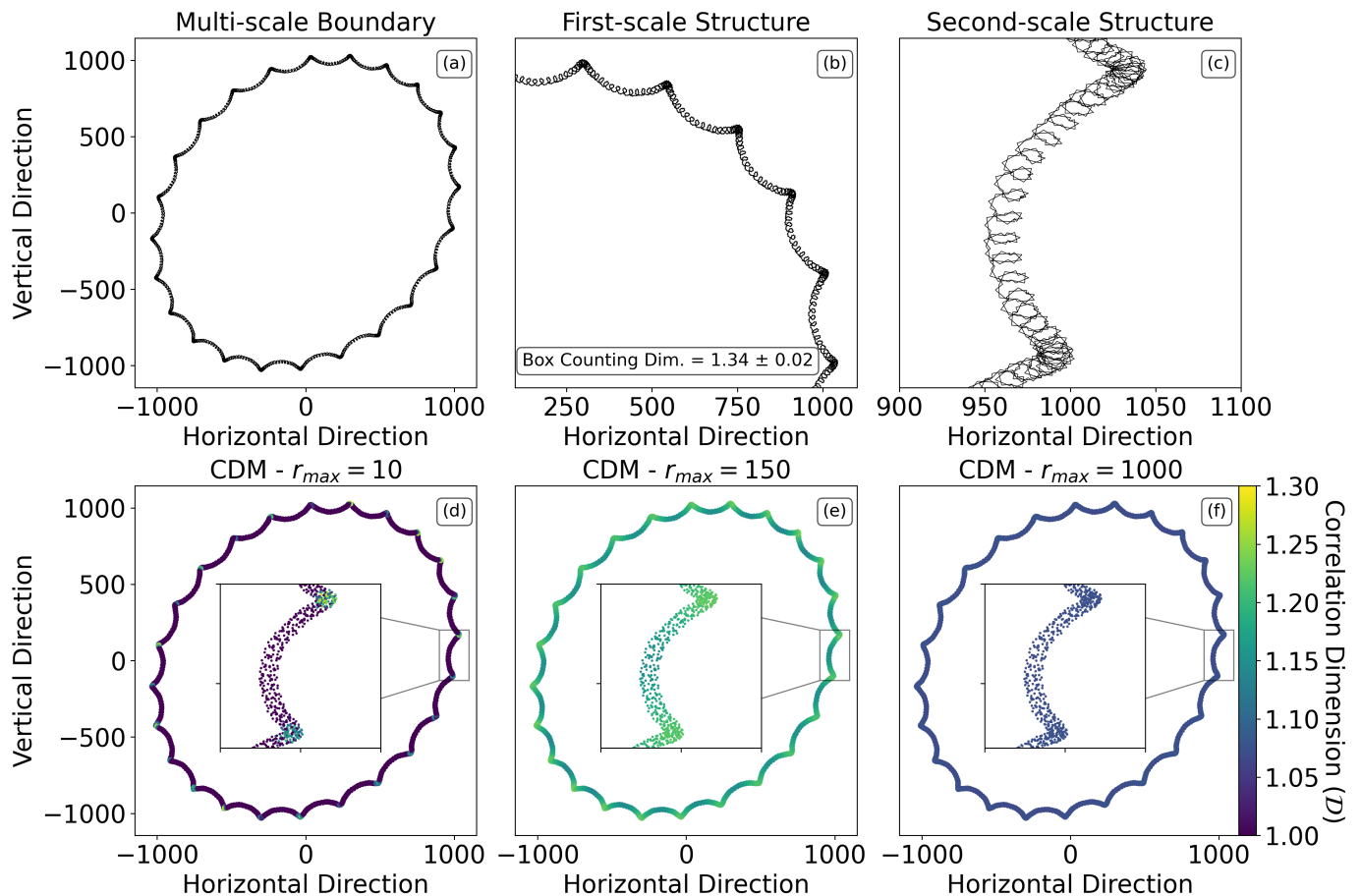


Figure 7. CDM on a synthetic multi-scale boundary and sensitivity to r_{\max} . (a–c) The boundary with multiple embedded spatial scales. (d–f) CDM results for $r_{\max} = \{10, 150, 1000\}$, illustrating how different scale ranges control the inferred \mathcal{D} values and identification of high-complexity regions

FRBLE extraction, we smooth the extracted boundary objects using a low-pass filter. Doing so reduces the spatial scales used to characterize the FRBLE substructures with CDM between 2.4 - 3.6 Mm (corresponding to local radii of 10 - 15 pixels of the IRIS-SJI camera, with 0.33 arcsecond resolution, at each boundary coordinate). DKIST Visible Broadband Imager (VBI; Wöger et al. 2021) observations have an expected spatial resolution of 0.017 arcseconds (Tamburri et al. 2025); thus, even when losing the same 10 pixels in the extraction of the FRBLE, it will still improve the lower bound of the spatial scales used in CDM to approximately 0.7 Mm. Furthermore, the spatial resolution of DKIST-VBI will improve the sampling of the spatial scales 20 times the current implementation, meaning DKIST-VBI can observe approximately 20 pixels per each IRIS-SJI pixel.

REFERENCES

- Afanasyev, A. N., Fan, Y., Kazachenko, M. D., & Cheung, M. C. M. 2023, *The Astrophysical Journal*, 952, 136, doi: [10.3847/1538-4357/acd7e9](https://doi.org/10.3847/1538-4357/acd7e9)
- Alexander, D., & Coyner, A. J. 2006, *The Astrophysical Journal*, 640, 505, doi: [10.1086/500076](https://doi.org/10.1086/500076)
- Alfvén, H. 1942, *Nature*, 150, 405, doi: [10.1038/150405d0](https://doi.org/10.1038/150405d0)
- Arnold, H., Drake, J. F., Swisdak, M., & Dahlin, J. 2019, *Physics of Plasmas*, 26, doi: [10.1063/1.5120373](https://doi.org/10.1063/1.5120373)
- Asai, A., Yokoyama, T., Shimojo, M., et al. 2004, *The Astrophysical Journal*, 611, 557, doi: [10.1086/422159](https://doi.org/10.1086/422159)
- Ashfield, W., Polito, V., Yu, S., Collier, H., & Hayes, L. A. 2024, *The Astrophysical Journal*, 973, 96, doi: [10.3847/1538-4357/ad64ca](https://doi.org/10.3847/1538-4357/ad64ca)
- Atwood, W. B., Abdo, A. A., Ackermann, M., et al. 2009, *Astrophysical Journal*, 697, 1071, doi: [10.1088/0004-637X/697/2/1071](https://doi.org/10.1088/0004-637X/697/2/1071)

- Aulanier, G., Démoulin, P., Schrijver, C. J., et al. 2013, *Astronomy & Astrophysics*, 549, A66, doi: [10.1051/0004-6361/201220406](https://doi.org/10.1051/0004-6361/201220406)
- Aulanier, G., Janvier, M., & Schmieder, B. 2012, *Astronomy & Astrophysics*, 543, A110, doi: [10.1051/0004-6361/201219311](https://doi.org/10.1051/0004-6361/201219311)
- Bacchini, F., Ruan, W., & Keppens, R. 2024, *Monthly Notices of the Royal Astronomical Society*, 529, 2399, doi: [10.1093/mnras/stae723](https://doi.org/10.1093/mnras/stae723)
- Bárta, M., Büchner, J., Karlický, M., & Kotrč, P. 2011, *The Astrophysical Journal*, 730, 47, doi: [10.1088/0004-637X/730/1/47](https://doi.org/10.1088/0004-637X/730/1/47)
- Benz, A. O. 2017, *Living Reviews in Solar Physics*, 14, doi: [10.1007/s41116-016-0004-3](https://doi.org/10.1007/s41116-016-0004-3)
- Bobra, M. G., Xudong, S., & Turmon, M. J. 2021, doi: [10.5281/ZENODO.5131292](https://doi.org/10.5281/ZENODO.5131292)
- Bornmann, P. L., Speich, D., Hirman, J., et al. 1996, in *GOES-8 and Beyond*, ed. E. R. Washwell, Vol. 2812 (SPIE), 291–298, doi: [10.1117/12.254076](https://doi.org/10.1117/12.254076)
- Bouligand, G. 1929, *Bull. Sci. Math.*, 2, 185
- Bradski, G. 2000, *Dr. Dobb's Journal of Software Tools*, 25, 122. <https://drdobbs.com/open-source/the-opencv-library/184404319?queryText=opencv>
- Brannon, S. R., Longcope, D. W., & Qiu, J. 2015, *The Astrophysical Journal*, 810, 4, doi: [10.1088/0004-637X/810/1/4](https://doi.org/10.1088/0004-637X/810/1/4)
- Brosius, J. W. 2012, *The Astrophysical Journal*, 754, 54, doi: [10.1088/0004-637X/754/1/54](https://doi.org/10.1088/0004-637X/754/1/54)
- Brown, J. C. 1971, *Solar Physics*, 18, 489, doi: [10.1007/BF00149070](https://doi.org/10.1007/BF00149070)
- Cannon, B., Jing, J., Li, Q., et al. 2023, *The Astrophysical Journal*, 950, 144, doi: [10.3847/1538-4357/accf9f](https://doi.org/10.3847/1538-4357/accf9f)
- Carmichael, H. 1964, in *The Physics of Solar Flares*, 451–456. <https://ui.adsabs.harvard.edu/abs/1964NASSP..50..451C/abstract>
- Cerutti, B., & Giacinti, G. 2021, *Astronomy & Astrophysics*, 656, A91, doi: [10.1051/0004-6361/202142178](https://doi.org/10.1051/0004-6361/202142178)
- Chamberlin, P. C., Woods, T. N., Eparvier, F. G., & Jones, A. R. 2009, in *Solar Physics and Space Weather Instrumentation III*, ed. S. Fineschi & J. A. Fennelly, Vol. 7438 (SPIE), 743802, doi: [10.1117/12.826807](https://doi.org/10.1117/12.826807)
- Chen, B., Bastian, T. S., Shen, C., et al. 2015, *Science*, 350, 1238, doi: [10.1126/science.aac8467](https://doi.org/10.1126/science.aac8467)
- Chen, B., Kong, X., Yu, S., et al. 2024, *The Astrophysical Journal*, 971, 85, doi: [10.3847/1538-4357/ad531a](https://doi.org/10.3847/1538-4357/ad531a)
- Cho, K., De Pontieu, B., & Testa, P. 2024, *The Astrophysical Journal*, 975, 33, doi: [10.3847/1538-4357/ad7586](https://doi.org/10.3847/1538-4357/ad7586)
- Clarke, B. P., Hayes, L. A., Gallagher, P. T., Maloney, S. A., & Carley, E. P. 2021, *The Astrophysical Journal*, 910, 123, doi: [10.3847/1538-4357/abe463](https://doi.org/10.3847/1538-4357/abe463)
- Collier, H., Hayes, L. A., Yu, S., et al. 2024, *Astronomy & Astrophysics*, 684, A215, doi: [10.1051/0004-6361/202348652](https://doi.org/10.1051/0004-6361/202348652)
- Comisso, L., Lingam, M., Huang, Y.-M., & Bhattacharjee, A. 2017, *The Astrophysical Journal*, 850, 142, doi: [10.3847/1538-4357/aa9789](https://doi.org/10.3847/1538-4357/aa9789)
- Corchado Albelo, M. F., Kazachenko, M. D., & Lynch, B. J. 2024, *The Astrophysical Journal*, 965, 16, doi: [10.3847/1538-4357/ad25f4](https://doi.org/10.3847/1538-4357/ad25f4)
- Dahlin, J. T., Antiochos, S. K., Wyper, P. F., Qiu, J., & DeVore, C. R. 2025, *The Astrophysical Journal*, 993, 31, doi: [10.3847/1538-4357/ae03c5](https://doi.org/10.3847/1538-4357/ae03c5)
- Dahlin, J. T., Drake, J. F., & Swisdak, M. 2017, *Physics of Plasmas*, 24, doi: [10.1063/1.4986211](https://doi.org/10.1063/1.4986211)
- Daughton, W., Roytershteyn, V., Karimabadi, H., et al. 2011, *Nature Physics*, 7, 539, doi: [10.1038/nphys1965](https://doi.org/10.1038/nphys1965)
- De Pontieu, B., Polito, V., Hansteen, V., et al. 2021, *Solar Physics*, 296, 84, doi: [10.1007/s11207-021-01826-0](https://doi.org/10.1007/s11207-021-01826-0)
- Démoulin, P., Priest, E. R., & Lonie, D. P. 1996, *Journal of Geophysical Research: Space Physics*, 101, 7631, doi: [10.1029/95JA03558](https://doi.org/10.1029/95JA03558)
- DeVore, C. R., & Antiochos, S. K. 2008, *The Astrophysical Journal*, 680, 740, doi: [10.1086/588011](https://doi.org/10.1086/588011)
- De Pontieu, B., Title, A. M., Lemen, J. R., et al. 2014, *Solar Physics*, 289, 2733, doi: [10.1007/s11207-014-0485-y](https://doi.org/10.1007/s11207-014-0485-y)
- Donnelly, R. F. 1971, *Solar Physics*, 20, 188, doi: [10.1007/BF00146110](https://doi.org/10.1007/BF00146110)
- Drake, J. F., Arnold, H., Swisdak, M., & Dahlin, J. T. 2019, *Physics of Plasmas*, 26, doi: [10.1063/1.5058140](https://doi.org/10.1063/1.5058140)
- Drake, J. F., Opher, M., Swisdak, M., & Chamoun, J. N. 2010, *The Astrophysical Journal*, 709, 963, doi: [10.1088/0004-637X/709/2/963](https://doi.org/10.1088/0004-637X/709/2/963)
- Drake, J. F., Swisdak, M., Che, H., & Shay, M. A. 2006, *Nature*, 443, 553, doi: [10.1038/nature05116](https://doi.org/10.1038/nature05116)
- Drake, J. F., Antiochos, S. K., Bale, S. D., et al. 2025, *Space Science Reviews*, 221, 27, doi: [10.1007/s11214-025-01153-x](https://doi.org/10.1007/s11214-025-01153-x)
- Druett, M., Ruan, W., & Keppens, R. 2024, *Astronomy & Astrophysics*, 684, A171, doi: [10.1051/0004-6361/202347600](https://doi.org/10.1051/0004-6361/202347600)
- Druett, M. K., Ruan, W., & Keppens, R. 2023, *Solar Physics*, 298, 134, doi: [10.1007/s11207-023-02224-4](https://doi.org/10.1007/s11207-023-02224-4)
- Fan, Y., Kazachenko, M. D., Afanasyev, A. N., & Fisher, G. H. 2024, *The Astrophysical Journal*, 975, 206, doi: [10.3847/1538-4357/ad7f53](https://doi.org/10.3847/1538-4357/ad7f53)

- Fielding, D. B., Ripperda, B., & Philippov, A. A. 2023, *The Astrophysical Journal Letters*, 949, L5, doi: [10.3847/2041-8213/accf1f](https://doi.org/10.3847/2041-8213/accf1f)
- Fletcher, L., & Hudson, H. 2001, *Solar Physics*, 204, 69, doi: [10.1023/A:1014275821318](https://doi.org/10.1023/A:1014275821318)
- Fletcher, L., & Hudson, H. S. 2008, *The Astrophysical Journal*, 675, 1645, doi: [10.1086/527044](https://doi.org/10.1086/527044)
- Forbes, T., & Lin, J. 2000, *Journal of Atmospheric and Solar-Terrestrial Physics*, 62, 1499, doi: [10.1016/S1364-6826\(00\)00083-3](https://doi.org/10.1016/S1364-6826(00)00083-3)
- Forbes, T. G. 2000, *Journal of Geophysical Research: Space Physics*, 105, 23153, doi: [10.1029/2000JA000005](https://doi.org/10.1029/2000JA000005)
- Forbes, T. G., & Priest, E. R. 1984, *Solar Physics*, 94, 315, doi: [10.1007/BF00151321](https://doi.org/10.1007/BF00151321)
- French, R. J., Ashfield, W. H., Tamburri, C. A., et al. 2025a, *The Astrophysical Journal*, 995, 182, doi: [10.3847/1538-4357/ae21b5](https://doi.org/10.3847/1538-4357/ae21b5)
- French, R. J., Hayes, L. A., Kazachenko, M. D., et al. 2024a, *The Astrophysical Journal*, 977, 207, doi: [10.3847/1538-4357/ad8ed1](https://doi.org/10.3847/1538-4357/ad8ed1)
- French, R. J., Matthews, S. A., Jonathan Rae, I., & Smith, A. W. 2021, *The Astrophysical Journal*, 922, 117, doi: [10.3847/1538-4357/ac256f](https://doi.org/10.3847/1538-4357/ac256f)
- French, R. J., Yu, S., Chen, B., Shen, C., & Matthews, S. A. 2024b, *Monthly Notices of the Royal Astronomical Society*, 528, 6836, doi: [10.1093/mnras/stae430](https://doi.org/10.1093/mnras/stae430)
- French, R. J., Kazachenko, M. D., Berghmans, D., et al. 2025b, *The Astrophysical Journal Letters*, 995, L54, doi: [10.3847/2041-8213/ae2684](https://doi.org/10.3847/2041-8213/ae2684)
- Furth, H. P., Killeen, J., & Rosenbluth, M. N. 1963, *Physics of Fluids*, 6, 459, doi: [10.1063/1.1706761](https://doi.org/10.1063/1.1706761)
- Gill, C. D., Fletcher, L., & Marshall, S. 2010, *Solar Physics*, 262, 355, doi: [10.1007/s11207-010-9508-5](https://doi.org/10.1007/s11207-010-9508-5)
- Goode, P., Coulter, R., Gorceix, N., Yurchyshyn, V., & Cao, W. 2010, *Astronomische Nachrichten*, 331, 620, doi: [10.1002/asna.201011387](https://doi.org/10.1002/asna.201011387)
- Gopalswamy, N., Makela, P., Akiyama, S., et al. 2018, *Journal of Atmospheric and Solar-Terrestrial Physics*, 179, 225, doi: [10.1016/j.jastp.2018.07.013](https://doi.org/10.1016/j.jastp.2018.07.013)
- Graham, D. R., & Cauzzi, G. 2015, *The Astrophysical Journal*, 807, L22, doi: [10.1088/2041-8205/807/2/L22](https://doi.org/10.1088/2041-8205/807/2/L22)
- Grassberger, P., & Procaccia, I. 1983, *Physica D: Nonlinear Phenomena*, 9, 189, doi: [10.1016/0167-2789\(83\)90298-1](https://doi.org/10.1016/0167-2789(83)90298-1)
- Guidoni, S. E., DeVore, C. R., Karpen, J. T., & Lynch, B. J. 2016, *The Astrophysical Journal*, 820, 60, doi: [10.3847/0004-637x/820/1/60](https://doi.org/10.3847/0004-637x/820/1/60)
- Guidoni, S. E., Karpen, J. T., & DeVore, C. R. 2022, *The Astrophysical Journal*, 925, 191, doi: [10.3847/1538-4357/ac39a5](https://doi.org/10.3847/1538-4357/ac39a5)
- Hayes, L. A., Gallagher, P. T., Dennis, B. R., et al. 2019, *arXiv*, 875, 33, doi: [10.3847/1538-4357/ab0ca3](https://doi.org/10.3847/1538-4357/ab0ca3)
- Heaviside, O. 2011, *Electrical Papers* (Cambridge University Press), doi: [10.1017/CBO9780511983139](https://doi.org/10.1017/CBO9780511983139)
- Hesse, M., Forbes, T. G., & Birn, J. 2005, *The Astrophysical Journal*, 631, 1227, doi: [10.1086/432677](https://doi.org/10.1086/432677)
- Hesse, M., & Schindler, K. 1988, *Journal of Geophysical Research: Space Physics*, 93, 5559, doi: [10.1029/JA093iA06p05559](https://doi.org/10.1029/JA093iA06p05559)
- Hirayama, T. 1974, *Solar Physics*, 34, 323, doi: [10.1007/BF00153671](https://doi.org/10.1007/BF00153671)
- Hoeksema, J. T., Liu, Y., Hayashi, K., et al. 2014, *Solar Physics*, 289, 3483, doi: [10.1007/s11207-014-0516-8](https://doi.org/10.1007/s11207-014-0516-8)
- Huang, C., Lu, Q., Wang, R., et al. 2017, *The Astrophysical Journal*, 835, 245, doi: [10.3847/1538-4357/835/2/245](https://doi.org/10.3847/1538-4357/835/2/245)
- Huang, K., Liu, Y., Lu, Q., et al. 2022, *Geophysical Research Letters*, 49, doi: [10.1029/2022GL100466](https://doi.org/10.1029/2022GL100466)
- Huang, Y.-M., & Bhattacharjee, A. 2012, *Physical Review Letters*, 109, 265002, doi: [10.1103/PhysRevLett.109.265002](https://doi.org/10.1103/PhysRevLett.109.265002)
- Huang, Z., Madjarska, M. S., Koleva, K., et al. 2014, *Astronomy & Astrophysics*, 566, A148, doi: [10.1051/0004-6361/201323097](https://doi.org/10.1051/0004-6361/201323097)
- Hudson, H. S. 2011, *Space Science Reviews*, 158, 5, doi: [10.1007/s11214-010-9721-4](https://doi.org/10.1007/s11214-010-9721-4)
- Janvier, M., Aulanier, G., Pariat, E., & Démoulin, P. 2013, *Astronomy & Astrophysics*, 555, A77, doi: [10.1051/0004-6361/201321164](https://doi.org/10.1051/0004-6361/201321164)
- Janvier, M., Savcheva, A., Pariat, E., et al. 2016, *Astronomy & Astrophysics*, 591, A141, doi: [10.1051/0004-6361/201628406](https://doi.org/10.1051/0004-6361/201628406)
- Jeffrey, N. L. S., Fletcher, L., Labrosse, N., & Simões, P. J. A. 2018, *Science Advances*, 4, doi: [10.1126/sciadv.aav2794](https://doi.org/10.1126/sciadv.aav2794)
- Jing, J., Xu, Y., Cao, W., et al. 2016, *Scientific Reports*, 6, 24319, doi: [10.1038/srep24319](https://doi.org/10.1038/srep24319)
- Karlický, M. 2014, *Research in Astronomy and Astrophysics*, 14, 753, doi: [10.1088/1674-4527/14/7/002](https://doi.org/10.1088/1674-4527/14/7/002)
- Karpen, J. T., Antiochos, S. K., & DeVore, C. R. 2012, *The Astrophysical Journal*, 760, 81, doi: [10.1088/0004-637X/760/1/81](https://doi.org/10.1088/0004-637X/760/1/81)
- Kazachenko, M. D., Albelo-Corchado, M. F., Tamburri, C. A., & Welsch, B. T. 2022, *Solar Physics*, 297, 59, doi: [10.1007/s11207-022-01987-6](https://doi.org/10.1007/s11207-022-01987-6)
- Kazachenko, M. D., Lynch, B. J., Welsch, B. T., & Sun, X. 2017, *The Astrophysical Journal*, 845, 49, doi: [10.3847/1538-4357/aa7ed6](https://doi.org/10.3847/1538-4357/aa7ed6)
- Keppens, R., Meliani, Z., van Marle, A., et al. 2012, *Journal of Computational Physics*, 231, 718, doi: [10.1016/j.jcp.2011.01.020](https://doi.org/10.1016/j.jcp.2011.01.020)

- Kerr, G. S., Carlsson, M., Allred, J. C., Young, P. R., & Daw, A. N. 2019, *The Astrophysical Journal*, 871, 23, doi: [10.3847/1538-4357/aaf46e](https://doi.org/10.3847/1538-4357/aaf46e)
- Kerr, G. S., Polito, V., Xu, Y., & Allred, J. C. 2024, *The Astrophysical Journal*, 970, 21, doi: [10.3847/1538-4357/ad47e1](https://doi.org/10.3847/1538-4357/ad47e1)
- Kerr, G. S., Xu, Y., Allred, J. C., et al. 2021, *The Astrophysical Journal*, 912, 153, doi: [10.3847/1538-4357/abf42d](https://doi.org/10.3847/1538-4357/abf42d)
- Kirk, M. S., Balasubramaniam, K. S., Jackiewicz, J., McNamara, B. J., & McAteer, R. T. J. 2013, *Solar Physics*, 283, 97, doi: [10.1007/s11207-011-9843-1](https://doi.org/10.1007/s11207-011-9843-1)
- Kitahara, T., & Kurokawa, H. 1990, *Solar Physics*, 125, 321, doi: [10.1007/BF00158409](https://doi.org/10.1007/BF00158409)
- Kliem, B., Karlický, M., & Benz, A. O. 2000, *Astron. Astrophys.*, 360, 715. <https://ui.adsabs.harvard.edu/abs/2000A%26A...360..715K/abstract>
- Kołodźński, S., & Karlický, M. 2007, *Astronomy & Astrophysics*, 475, 685, doi: [10.1051/0004-6361:20078356](https://doi.org/10.1051/0004-6361:20078356)
- Kong, X., Guo, F., Shen, C., et al. 2020, *The Astrophysical Journal Letters*, 905, L16, doi: [10.3847/2041-8213/abcbf5](https://doi.org/10.3847/2041-8213/abcbf5)
- Kopp, R., & Pneuman, G. 1976, *Solar Physics*, 50, doi: [10.1007/BF00206193](https://doi.org/10.1007/BF00206193)
- Kowalski, A. F., Allred, J. C., Daw, A., Cauzzi, G., & Carlsson, M. 2017, *The Astrophysical Journal*, 836, 12, doi: [10.3847/1538-4357/836/1/12](https://doi.org/10.3847/1538-4357/836/1/12)
- Kumar, P., Karpen, J. T., & Dahlin, J. T. 2025, *The Astrophysical Journal*, 980, 158, doi: [10.3847/1538-4357/ada293](https://doi.org/10.3847/1538-4357/ada293)
- Kuroda, N., Gary, D. E., Wang, H., et al. 2018, *The Astrophysical Journal*, 852, 32, doi: [10.3847/1538-4357/aa9d98](https://doi.org/10.3847/1538-4357/aa9d98)
- Kurokawa, H., Takakura, T., & Ohki, K. 1988, *Publications of the Astronomical Society of Japan*, 40, 357, doi: [10.1093/pasj/40.3.357](https://doi.org/10.1093/pasj/40.3.357)
- Lemen, J. R., Title, A. M., Akin, D. J., et al. 2012, *Solar Physics*, 275, 17, doi: [10.1007/s11207-011-9776-8](https://doi.org/10.1007/s11207-011-9776-8)
- Li, T., & Zhang, J. 2015, *The Astrophysical Journal*, 804, L8, doi: [10.1088/2041-8205/804/1/L8](https://doi.org/10.1088/2041-8205/804/1/L8)
- Li, X., Shen, C., Xie, X., et al. 2025, *The Astrophysical Journal*, 991, 202, doi: [10.3847/1538-4357/adfed5](https://doi.org/10.3847/1538-4357/adfed5)
- Li, Y., Sun, X., Ding, M. D., Qiu, J., & Priest, E. R. 2017, *The Astrophysical Journal*, 835, 190, doi: [10.3847/1538-4357/835/2/190](https://doi.org/10.3847/1538-4357/835/2/190)
- Longcope, D., Beveridge, C., Qiu, J., et al. 2007, *Solar Physics*, 244, 45, doi: [10.1007/s11207-007-0330-7](https://doi.org/10.1007/s11207-007-0330-7)
- Longcope, D. W. 2014, *The Astrophysical Journal*, 795, 10, doi: [10.1088/0004-637X/795/1/10](https://doi.org/10.1088/0004-637X/795/1/10)
- Lörinčík, J., Polito, V., De Pontieu, B., Yu, S., & Freij, N. 2022, *Frontiers in Astronomy and Space Sciences*, 9, doi: [10.3389/fspas.2022.1040945](https://doi.org/10.3389/fspas.2022.1040945)
- Loureiro, N. F., Schekochihin, A. A., College, K., & Cowley, S. C. 2007, *Physics of Plasmas*, 14, doi: [10.1063/1.2783986](https://doi.org/10.1063/1.2783986)
- Lu, L., Feng, L., Warmuth, A., et al. 2022, *The Astrophysical Journal Letters*, 924, L7, doi: [10.3847/2041-8213/ac42c6](https://doi.org/10.3847/2041-8213/ac42c6)
- Lynch, B. J., Edmondson, J. K., Kazachenko, M. D., & Guidoni, S. E. 2016, *The Astrophysical Journal*, 826, 43, doi: [10.3847/0004-637X/826/1/43](https://doi.org/10.3847/0004-637X/826/1/43)
- Machol, J. L., Eparvier, F. G., Viereck, R. A., et al. 2019, in *The GOES-R Series: A New Generation of Geostationary Environmental Satellites* (Elsevier), 233–242, doi: [10.1016/B978-0-12-814327-8.00019-6](https://doi.org/10.1016/B978-0-12-814327-8.00019-6)
- Magara, T., Mineshige, S., Yokoyama, T., & Shibata, K. 1996, *The Astrophysical Journal*, 466, 1054, doi: [10.1086/177575](https://doi.org/10.1086/177575)
- Marr, D., & Hildreth, E. 1980, *Proceedings of the Royal Society of London. Series B. Biological Sciences*, 207, 187, doi: [10.1098/rspb.1980.0020](https://doi.org/10.1098/rspb.1980.0020)
- Mason, E. I., & Uritsky, V. M. 2022, *The Astrophysical Journal Letters*, 937, L19, doi: [10.3847/2041-8213/ac9124](https://doi.org/10.3847/2041-8213/ac9124)
- Maurya, R. A., & Ambastha, A. 2010, *Solar Physics*, 262, 337, doi: [10.1007/s11207-009-9488-5](https://doi.org/10.1007/s11207-009-9488-5)
- Meegan, C., Lichti, G., Bhat, P. N., et al. 2009, *Astrophysical Journal*, 702, 791, doi: [10.1088/0004-637X/702/1/791](https://doi.org/10.1088/0004-637X/702/1/791)
- Milligan, R. O., McAteer, R. T. J., Dennis, B. R., & Young, C. A. 2010, *The Astrophysical Journal*, 713, 1292, doi: [10.1088/0004-637X/713/2/1292](https://doi.org/10.1088/0004-637X/713/2/1292)
- Minkowski, H. 1901, *Jahresbericht der Deutschen Mathematiker-Vereinigung*, 1, 115. <http://eudml.org/doc/144684>
- Müller, D., St. Cyr, O. C., Zouganelis, I., et al. 2020, *Astronomy & Astrophysics*, 642, A1, doi: [10.1051/0004-6361/202038467](https://doi.org/10.1051/0004-6361/202038467)
- Nakamura, R., Burch, J. L., Birn, J., et al. 2025, *Space Science Reviews*, 221, 17, doi: [10.1007/s11214-025-01143-z](https://doi.org/10.1007/s11214-025-01143-z)
- Nakariakov, V. M., & Melnikov, V. F. 2009, *Space Science Reviews*, 149, 119, doi: [10.1007/s11214-009-9536-3](https://doi.org/10.1007/s11214-009-9536-3)
- Naus, S. J., Qiu, J., DeVore, C. R., et al. 2022, *The Astrophysical Journal*, 926, 218, doi: [10.3847/1538-4357/ac4028](https://doi.org/10.3847/1538-4357/ac4028)
- Nishizuka, N., Asai, A., Takasaki, H., Kurokawa, H., & Shibata, K. 2009, *The Astrophysical Journal*, 694, L74, doi: [10.1088/0004-637X/694/1/L74](https://doi.org/10.1088/0004-637X/694/1/L74)

- Nyquist, H. 1928, *Transactions of the American Institute of Electrical Engineers*, 47, 617, doi: [10.1109/T-AIEE.1928.5055024](https://doi.org/10.1109/T-AIEE.1928.5055024)
- Ohyama, M., & Shibata, K. 1998, *The Astrophysical Journal*, 499, 934, doi: [10.1086/305652](https://doi.org/10.1086/305652)
- Olson, J., Egedal, J., Greess, S., et al. 2016, *Physical Review Letters*, 116, 255001, doi: [10.1103/PhysRevLett.116.255001](https://doi.org/10.1103/PhysRevLett.116.255001)
- Parker, J., & Longcope, D. 2017, *The Astrophysical Journal*, 847, 30, doi: [10.3847/1538-4357/aa8908](https://doi.org/10.3847/1538-4357/aa8908)
- Pesnell, W. D., Thompson, B. J., & Chamberlin, P. C. 2012, *Solar Physics*, 275, 3, doi: [10.1007/s11207-011-9841-3](https://doi.org/10.1007/s11207-011-9841-3)
- Pietrow, A. G. M., Druett, M. K., & Singh, V. 2024, *Astronomy & Astrophysics*, 685, A137, doi: [10.1051/0004-6361/202348839](https://doi.org/10.1051/0004-6361/202348839)
- Polito, V., Kerr, G. S., Xu, Y., Sadykov, V. M., & Lorincik, J. 2023, *The Astrophysical Journal*, 944, 104, doi: [10.3847/1538-4357/aca77c](https://doi.org/10.3847/1538-4357/aca77c)
- Priest, E., & Forbes, T. 2002, *The Astronomy and Astrophysics Review*, 10, 313, doi: [10.1007/s001590100013](https://doi.org/10.1007/s001590100013)
- Priest, E. R., & Démoulin, P. 1995, *Journal of Geophysical Research: Space Physics*, 100, 23443, doi: [10.1029/95JA02740](https://doi.org/10.1029/95JA02740)
- Priest, E. R., & Forbes, T. G. 1992, *Journal of Geophysical Research: Space Physics*, 97, 1521, doi: [10.1029/91JA02435](https://doi.org/10.1029/91JA02435)
- Priest, E. R., & Longcope, D. W. 2017, *Solar Physics*, 292, 25, doi: [10.1007/s11207-016-1049-0](https://doi.org/10.1007/s11207-016-1049-0)
- Purkhart, S., Collier, H., Hayes, L. A., et al. 2025, *Astronomy & Astrophysics*, 698, A318, doi: [10.1051/0004-6361/202554475](https://doi.org/10.1051/0004-6361/202554475)
- Qiu, J., Liu, W.-J., & Longcope, D. W. 2012, *The Astrophysical Journal*, 752, 124, doi: [10.1088/0004-637X/752/2/124](https://doi.org/10.1088/0004-637X/752/2/124)
- Qiu, J., Wang, H., Cheng, C. Z., & Gary, D. E. 2004, *The Astrophysical Journal*, 604, 900, doi: [10.1086/382122](https://doi.org/10.1086/382122)
- Qu, M., Shih, F. Y., Jing, J., & Wang, H. 2003, *Solar Physics*, 217, 157, doi: [10.1023/A:1027388729489](https://doi.org/10.1023/A:1027388729489)
- Ramaty, R., & Mandzhavidze, N. 2000, in *AIP Conference Proceedings (AIP)*, 401–410, doi: [10.1063/1.1291742](https://doi.org/10.1063/1.1291742)
- Reep, J. W., & Russell, A. J. B. 2016, *The Astrophysical Journal Letters*, 818, L20, doi: [10.3847/2041-8205/818/1/L20](https://doi.org/10.3847/2041-8205/818/1/L20)
- Rimmele, T. R., Warner, M., Keil, S. L., et al. 2020, *Solar Physics*, 295, 172, doi: [10.1007/s11207-020-01736-7](https://doi.org/10.1007/s11207-020-01736-7)
- Ripperda, B., Liska, M., Chatterjee, K., et al. 2022, *The Astrophysical Journal Letters*, 924, L32, doi: [10.3847/2041-8213/ac46a1](https://doi.org/10.3847/2041-8213/ac46a1)
- Savcheva, A., Pariat, E., McKillop, S., et al. 2016, *The Astrophysical Journal*, 817, 43, doi: [10.3847/0004-637X/817/1/43](https://doi.org/10.3847/0004-637X/817/1/43)
- . 2015, *The Astrophysical Journal*, 810, 96, doi: [10.1088/0004-637X/810/2/96](https://doi.org/10.1088/0004-637X/810/2/96)
- Savcheva, A., Pariat, E., van Ballegooijen, A., Aulanier, G., & DeLuca, E. 2012, *The Astrophysical Journal*, 750, 15, doi: [10.1088/0004-637X/750/1/15](https://doi.org/10.1088/0004-637X/750/1/15)
- Schindler, K., Hesse, M., & Birn, J. 1988, *Journal of Geophysical Research: Space Physics*, 93, 5547, doi: [10.1029/JA093iA06p05547](https://doi.org/10.1029/JA093iA06p05547)
- Schmidt, D., Rimmele, T. R., & Gorceix, N. 2018, in *Adaptive Optics Systems VI*, ed. D. Schmidt, L. Schreiber, & L. M. Close (SPIE), 211, doi: [10.1117/12.2312888](https://doi.org/10.1117/12.2312888)
- Schmidt, D., Schad, T. A., Yurchyshyn, V., et al. 2025, *Nature Astronomy*, doi: [10.1038/s41550-025-02564-0](https://doi.org/10.1038/s41550-025-02564-0)
- Shannon, C. 1949, *Proceedings of the IRE*, 37, 10, doi: [10.1109/JRPROC.1949.232969](https://doi.org/10.1109/JRPROC.1949.232969)
- Shen, C., Chen, B., Reeves, K. K., et al. 2022, *Nature Astronomy*, 6, 317, doi: [10.1038/s41550-021-01570-2](https://doi.org/10.1038/s41550-021-01570-2)
- Shen, C., Polito, V., Reeves, K. K., et al. 2023, *Frontiers in Astronomy and Space Sciences*, 10, doi: [10.3389/fspas.2023.1096133](https://doi.org/10.3389/fspas.2023.1096133)
- Shibata, K., & Magara, T. 2011, *Living Reviews in Solar Physics*, 8, doi: [10.12942/lrsp-2011-6](https://doi.org/10.12942/lrsp-2011-6)
- Shibata, K., Takasao, S., & Reeves, K. K. 2023, *The Astrophysical Journal*, 943, 106, doi: [10.3847/1538-4357/aca9c](https://doi.org/10.3847/1538-4357/aca9c)
- Shibata, K., & Tanuma, S. 2001, *Earth, Planets and Space*, 53, 473, doi: [10.1186/BF03353258](https://doi.org/10.1186/BF03353258)
- Somov, B. 2006, in *Plasma Astrophysics, Part II*, Vol. 341 (New York: Springer), 193–204, doi: [10.1007/978-0-387-68894-7_{_}12](https://doi.org/10.1007/978-0-387-68894-7_{_}12)
- Spearman, C. 1904, *The American Journal of Psychology*, 15, 72, doi: [10.2307/1412159](https://doi.org/10.2307/1412159)
- Sturrock, P. A. 1966, *Nature*, 211, 695, doi: [10.1038/211695a0](https://doi.org/10.1038/211695a0)
- Sun, X. 2013. <http://arxiv.org/abs/1309.2392>
- Takasao, S., Asai, A., Isobe, H., & Shibata, K. 2012, *The Astrophysical Journal*, 745, L6, doi: [10.1088/2041-8205/745/1/L6](https://doi.org/10.1088/2041-8205/745/1/L6)
- Tamburri, C. A., Kazachenko, M. D., Cauzzi, G., et al. 2025, *The Astrophysical Journal Letters*, 990, L3, doi: [10.3847/2041-8213/adf95e](https://doi.org/10.3847/2041-8213/adf95e)
- Thoen Faber, J., Joshi, R., van der Voort, L. R., et al. 2025, *Astronomy & Astrophysics*, 693, A8, doi: [10.1051/0004-6361/202452370](https://doi.org/10.1051/0004-6361/202452370)

- Uzdensky, D. A., Loureiro, N. F., & Schekochihin, A. A. 2010, *Physical Review Letters*, 105, doi: [10.1103/PhysRevLett.105.235002](https://doi.org/10.1103/PhysRevLett.105.235002)
- Virtanen, P., Gommers, R., Oliphant, T. E., et al. 2020, *Nature Methods*, 17, 261, doi: [10.1038/s41592-019-0686-2](https://doi.org/10.1038/s41592-019-0686-2)
- Wang, Y., Cheng, X., & Ding, M. 2025, *The Astrophysical Journal*, 985, 43, doi: [10.3847/1538-4357/adca3d](https://doi.org/10.3847/1538-4357/adca3d)
- Wang, Y., Cheng, X., Ding, M., et al. 2023, *The Astrophysical Journal Letters*, 954, L36, doi: [10.3847/2041-8213/acf19d](https://doi.org/10.3847/2041-8213/acf19d)
- Warren, H. P., & Warshall, A. D. 2001, *The Astrophysical Journal*, 560, L87, doi: [10.1086/324060](https://doi.org/10.1086/324060)
- Weierstraß, K. 1988, in *Ausgewählte Kapitel aus der Funktionenlehre* (Wiesbaden: Vieweg+Teubner Verlag), 190–193, doi: [10.1007/978-3-322-91273-2_{-}5](https://doi.org/10.1007/978-3-322-91273-2_{-}5)
- Wöger, F., Rimmele, T., Ferayorni, A., et al. 2021, *Solar Physics*, 296, 145, doi: [10.1007/s11207-021-01881-7](https://doi.org/10.1007/s11207-021-01881-7)
- Wyper, P. F., & Hesse, M. 2015, *Physics of Plasmas*, 22, doi: [10.1063/1.4918335](https://doi.org/10.1063/1.4918335)
- Wyper, P. F., & Pontin, D. I. 2021, *The Astrophysical Journal*, 920, 102, doi: [10.3847/1538-4357/ac1943](https://doi.org/10.3847/1538-4357/ac1943)
- Xie, X., Shen, C., Reeves, K. K., et al. 2025, *The Astrophysical Journal Letters*, 984, L27, doi: [10.3847/2041-8213/adc91b](https://doi.org/10.3847/2041-8213/adc91b)
- Yadav, R., Kazachenko, M. D., Cauzzi, G., et al. 2025, *The Astrophysical Journal*, doi: [10.3847/1538-4357/adf4c1](https://doi.org/10.3847/1538-4357/adf4c1)
- Yang, M., Tian, Y., Liu, Y., & Rao, C. 2018, *Solar Physics*, 293, 81, doi: [10.1007/s11207-018-1300-y](https://doi.org/10.1007/s11207-018-1300-y)
- Zhao, Z., An, H., Xie, Y., et al. 2022, *Communications Physics*, 5, 247, doi: [10.1038/s42005-022-01026-7](https://doi.org/10.1038/s42005-022-01026-7)